Aerosol Science and Technology

ISSN: 0278-6826 (Print) 1521-7388 (Online) Journal homepage: http://www.tandfonline.com/loi/uast20

Design, simulation, and characterization of a radial opposed migration ion and aerosol classifier (ROMIAC)

Wilton Mui, Huajun Mai, Andrew J. Downard, John H. Seinfeld & Richard C. Flagan

To cite this article: Wilton Mui, Huajun Mai, Andrew J. Downard, John H. Seinfeld & Richard C. Flagan (2017): Design, simulation, and characterization of a radial opposed migration ion and aerosol classifier (ROMIAC), Aerosol Science and Technology, DOI: 10.1080/02786826.2017.1315046

To link to this article: http://dx.doi.org/10.1080/02786826.2017.1315046

AEROSOL SCIENCE AND TECHNOLOGY
http://dx.doi.org/10.1080/02786826.2017.1315046

Design, simulation, and characterization of a radial opposed migration ion and aerosol classifier (ROMIAC)

Wilton Mui [a], Huajun Mai[a], Andrew J. Downard[b], John H. Seinfeld[a,b], and Richard C. Flagan [a,b]

[a]Division of Engineering and Applied Science, California Institute of Technology, Pasadena, California, USA; [b]Division of Chemistry and Chemical Engineering, California Institute of Technology, Pasadena, California, USA

ABSTRACT

We present the design, simulation, and characterization of the radial opposed migration ion and aerosol classifier (ROMIAC), a compact differential electrical mobility classifier. We evaluate the performance of the ROMIAC using a combination of finite element modeling and experimental validation of two nearly identical instruments using tetra-alkyl ammonium halide mass standards and sodium chloride particles. Mobility and efficiency calibrations were performed over a wide range of particle diameters and flow rates to characterize ROMIAC performance under the range of anticipated operating conditions. The ROMIAC performs as designed, though performance deviates from that predicted using simplistic models of the instrument. The underlying causes of this non-ideal behavior are found through finite element simulations that predict the performance of the ROMIAC with greater accuracy than the simplistic models. It is concluded that analytical performance models based on idealized geometries, flows, and fields should not be relied on to make accurate *a priori* predictions about instrumental behavior if the actual geometry or fields deviate from the ideal assumptions. However, if such deviations are accurately captured, finite element simulations have the potential to predict instrumental performance. The present prototype of the ROMIAC maintains its resolution over nearly three orders of magnitude in particle mobility, obtaining sub-20 nm particle size distributions in a compact package with relatively low flow rate operation requirements.

ARTICLE HISTORY
Received 5 June 2016
Accepted 1 February 2017

EDITOR
Jian Wang

1. Introduction

1.1. Differential mobility analyzer

The differential mobility analyzer (DMA) has long been the primary instrument used to measure size distributions of aerosol particles smaller than 1 μm in diameter. This instrument separates charged particles according to their electrical mobilities, Z, in an electric field that is transverse to a particle-free sheath flow (Knutson and Whitby 1975). Particles within a narrow range of mobilities migrate across a channel between two electrodes in the time required to transit the length from the entrance port to a downstream sample extraction port in the counter-electrode, where they exit in a classified sample flow; others deposit on the walls of the DMA or are discharged in an exhaust flow.

In the ideal, non-diffusive limit, the range of particle mobilities in the classified sample flow is determined by the relative aerosol and sheath flow rates (Knutson and Whitby 1975). The most common DMA is that of Knutson and Whitby, which probes particles ranging from 10 to 1000 nm in mobility-equivalent diameter, D_Z, though the range that can be scanned with reasonable size resolution is narrower unless the flow rates are varied. Earlier DMAs had probed molecular ions, e.g., see Erikson (1921) and Flagan (1998). The Knutson-Whitby DMA (KWDMA) is usually operated with sheath and exhaust flow rates (Q_{sh} and Q_{ex}, respectively) 10 times those of the aerosol and classified sample flows (Q_a and Q_c). The operating conditions of the DMA are generally described in terms of the flow rate ratio $\beta = (Q_a + Q_c)/(Q_{sh} + Q_{ex})$, which is the primary factor determining the resolving power of the instrument, and $\delta = (Q_c - Q_a)/(Q_c + Q_a)$, a measure of the flow imbalance. DMAs are typically operated with balanced flows, i.e., $Q_a = Q_c$ and $\delta = 0$.

The performance of a DMA is conveniently described in terms of the transfer function, which is defined as the probability that a particle of mobility Z will be

CONTACT Richard C. Flagan flagan@caltech.edu Division of Engineering and Applied Science, California Institute of Technology Pasadena, CA 91125, USA and Division of Chemistry and Chemical Engineering, California Institute of Technology, Pasadena, CA 91125, USA.

Color versions of one or more of the figures in the article can be found online at www.tandfonline.com/uast

Supplemental data for this article can be accessed on the publisher's website.

transmitted through the classifier when the voltage and flow rates are tuned to transmit particles of characteristic mobility Z^*, which corresponds to particles that enter the classifier at the centroid of the incoming aerosol sample flow, and exit at the centroid of the outgoing classified aerosol flow. In their landmark paper, Knutson and Whitby (1975) employed fluid and particle stream functions to derive the so-called transfer function for particles that do not diffuse as they transit the DMA. The fluid stream function, ψ, is defined such that

$$ru_r = \frac{\partial \psi}{\partial z}, \quad \text{and} \quad ru_z = -\frac{\partial \psi}{\partial r} \qquad [1]$$

(where r is the classifier radial coordinate, z is the classifier axial coordinate, and u_r and u_z are the radial and axial fluid velocities, respectively); the stream function automatically satisfies the mass continuity for the gas. Particles of electrical mobility Z also migrate at velocity $\vec{v}$ under the action of the applied electric field, i.e., $\vec{v} = Z\,\vec{E}$. This migration can be described in terms of the electric flux function, ϕ, which is defined such that

$$rE_r = \frac{\partial \phi}{\partial z}, \quad \text{and} \quad rE_z = -\frac{\partial \phi}{\partial r}. \qquad [2]$$

For a steady electric field, a pseudo-steady-state can be assumed for the particle motion, so these contributions to the particle motion can be described in terms of a particle stream function (Knutson and Whitby 1975; Stolzenburg 1988), which is defined as

$$\Gamma = \psi + Z\phi. \qquad [3]$$

When particles are sufficiently large that diffusion can be neglected, particles follow trajectories along which $\Gamma =$ constant, though both ψ and ϕ change along the migration trajectory, so

$$\Gamma_{out} - \Gamma_{in} = \Delta\Gamma = 0 = \Delta\psi + Z\Delta\phi. \qquad [4]$$

Thus, Knutson and Whitby (1975) noted that the migration of particles across a range of stream functions, $\Delta\psi$, requires that it also migrate across a range of electric flux functions, $\Delta\phi = -\Delta\psi/Z$. The volumetric flow rate, Q, between the outer electrode, R_2, and a radial position, r, is $Q(r) = \int_r^{R_2} [2\pi r u_z(r)]\mathrm{d}r = 2\pi[\psi(r) - \psi_1]$, where ψ_1 is the value of the stream function at the aerosol-inlet electrode. Hereafter, we define $\psi_1 = 0$. They further derive the centroid of the DMA transfer function as that for which a non-diffusive particle will be transmitted from the radial position at which 50% of the cumulative incoming aerosol flow enters to the corresponding 50% radius for the cumulative classified aerosol outlet flow. We label the trajectory of these particles as the characteristic trajectory for the DMA. The mobility of the particle that follows this 50%–50% trajectory is denoted as Z^*. The range of stream function values crossed is defined by the specified inlet and outlet flow fractions, i.e., $\psi^*_{in} = Q_a/4\pi$, and $\psi^*_{out} = (Q_{sh} + Q_{ex} + Q_a)/4\pi$; thus,

$$\Delta\psi^* = \frac{Q_{sh} + Q_{ex}}{4\pi}. \qquad [5]$$

The change in electric flux function that a particle traverses, $\Delta\phi^*$, depends upon the spatial variation of the electric field. In the special case of a long, cylindrical DMA column, for which the aspect ratio $\alpha = L/(R_2 - R_1) \gg 1$, where L is the axial length of the electrode, the electric field can be assumed to be perpendicular to the electrode surfaces, i.e., $E_r = -\frac{V}{r\ln\frac{R_2}{R_1}}$ and $E_z = 0$, where V is the voltage applied to the central electrode, and R_1 and R_2 are the radii of the inner electrode and the outer electrode, respectively. Then,

$$\Delta\phi^*|_{\alpha\gg1} = -\frac{VL}{\ln\frac{R_2}{R_1}}, \qquad [6]$$

and, since $Z^* = -\frac{\Delta\psi^*}{\Delta\phi^*}$, we find

$$Z^*_{CDMA,\alpha\gg1} = \frac{(Q_{sh} + Q_{ex})}{4\pi VL}\ln\frac{R_2}{R_1}. \qquad [7]$$

In this special case, the transmission characteristics of such a classifier can be determined to a high degree of accuracy from first principles with simple analytic expressions. The DMA can then be considered to provide a primary particle *mobility* standard, at least for large, non-diffusive particles. Stolzenburg (1988; see also Flagan 1999) showed that particles that are transmitted at high voltage satisfy this large particle condition. Moreover, for spherical particles, the DMA becomes a primary particle *size* standard since the electrical mobility is a well-known function of particle diameter.

Rather than focusing on the absolute sizing accuracy, most recent DMA characterization studies have focused on the resolution of the instrument, $\mathcal{R}$, which is defined as the ratio of the mobility of the particles that are transmitted with the highest efficiency, Z_{peak}, to the range of mobilities that are transmitted with at least half of that efficiency, i.e., $\mathcal{R} = Z_{peak}/\Delta Z_{50\%}$. At high classification voltage in long-column cylindrical DMAs, $Z_{peak} \approx Z^*$. When classifying large particles (at high voltage), the resolution approaches the asymptotic limit for ideal, non-diffusive (kinematic) classification determined using the triangular transfer function of Knutson and Whitby (1975) for balanced flows, $\delta = 0$ (trapezoidal if $\delta \neq 0$). In this limit, the non-diffusive (large particle) resolution for

a DMA is

$$\mathcal{R}_{\mathrm{nd}} = \left[\beta(1+|\delta|)\right]^{-1}, \qquad [8]$$

and the peak transmission efficiency for a DMA operated at constant voltage occurs for particles of mobility Z^*.

1.2. Advancing nanometer particle classification

Over the past two and a half decades, a number of innovations have extended the classification capabilities of the DMA to smaller particles, beginning with the Vienna short-column DMA that enabled measurements of particles as small as 3.5 nm (Winklmayr et al. 1991). Other designs have been developed to probe the sub-10 nm range. These include adaptations of the Knutson and Whitby DMA to produce the nanoDMA (Chen et al. 1998), and the radial DMA (RDMA; Zhang et al. 1995). Development has continued, enabling classification of particles as small as 1 nm (Rosell-Llompart et al. 1996; Labowsky and de la Mora 2006; Brunelli et al. 2009).

The ability to classify particles in the low-nanometer regime enabled measurements of gas ions and stimulated efforts to develop instruments that attain much higher resolution than traditional DMAs for applications in molecular separations. de la Mora and coworkers (Rosser and de la Mora 2005; Martínez-Lozano and de la Mora 2006; Martínez-Lozano et al. 2006) have demonstrated DMAs that attain $\mathcal{R} \sim 100$ at voltages near the electrostatic breakdown (arcing) limit, albeit over a very limited range of mobilities. To achieve this resolution, these DMAs operate at Reynolds numbers well beyond that typically associated with the onset of turbulence. Although the exceptionally high flow rates required for these supercritical, laminar-flow, high-resolution DMAs (100 to 1000 liters per minute (lpm) or more) limit their applicability, these instruments have enabled a number of important studies, especially when used as a front-end to a mass spectrometer (Hogan and de la Mora 2010; Rus et al. 2010; Hogan and de la Mora 2011; Oberreit et al. 2015).

A key feature of DMAs that extend the sizing range to the low nanometer regime is the use of a low aspect ratio classifier, i.e., $\alpha = \frac{\text{length of classification region}}{\text{migration distance between electrodes}} \sim 1$ (Rosell-Llompart et al. 1996). While some such instruments have maintained electric fields perpendicular to the electrodes, others have not, leading to electric fields that vary with both r and z. The value of $\Delta\psi^*$ in such instruments is still that specified by the Knutson and Whitby definition of the characteristic particle streamline, but the presence of both radial and axial components to the electric field may preclude simple, analytical expressions for $\Delta\phi^*$. Instead, $\Delta\phi^*$ may be determined numerically or by calibration with suitable mobility standards. Deviations from the value of Z^*_{ideal} suggested by idealized, i.e., high aspect ratio, models have been reported by introducing an empirical mobility correction factor, f_Z, thereby accounting for both the low aspect ratio perturbations to fields and the effects of imperfections in the instrument, i.e.,

$$Z^* = f_Z Z^*_{\mathrm{ideal}} = -\frac{f_Z \Delta\psi^*}{\Delta\phi^*}. \qquad [9]$$

Since $\Delta\psi^*$ is specified by the Knutson and Whitby analysis, i.e., Equation (9), Z^* gives an estimate of $\Delta\phi^*$, provided the calibration is performed using mobility standards that are large enough that they require voltages well beyond the diffusional broadening threshold (Flagan 1999). The transfer function for DMA classification of diffusive particles is well described by the semi-analytical model of Stolzenburg (1988), even for DMAs that deviate from those with idealized fields.

While particles in the low-nanometer regime can be classified with DMAs, transmission efficiencies are often quite low at the smallest particle sizes because of high diffusional losses. A recent intercomparison of several nanoparticle DMAs found transmission efficiencies of 1.16 nm particles that ranged from nondetectable to as high as 17% (Jiang et al. 2011). Diffusional losses in DMAs are accentuated by adverse potential gradients in the transition between the grounded exterior plumbing and the high voltage electrode. Depending on the DMA design, this adverse gradient may occur at either the entrance or exit of the DMA, but it is present in *nearly* all DMA designs. However, by careful design of those regions of the DMA, the effect of the adverse potential gradient can be reduced (Kousaka et al. 1986; Zhang and Flagan 1996; Franchin et al. 2016). While the adverse gradient is integral to the design of all commonly used DMAs, Labowsky and de la Mora (2006) described a novel instrument in which particles are introduced and extracted from the grounded side of the classifier; that classifier can, however, only be used with an electrometer or other charged particle detector because neutral particles will be included in the classified-sample outlet flow. Tammet demonstrated a highly modified DMA in which the field is created by applying a potential between a pair of screens that are inclined with respect to the sheath flow (Tammet 2003, 2011). This symmetric inclined grid mobility analyzer classifies ions and particles of both polarities (hence "symmetric") in the 0.4–7.5 nm range with $\mathcal{R}$ of 2–3.

Yet another approach to classifying particles is the transient drift-tube ion-mobility spectrometer of Oberreit et al. (2014). In this device, a bolus of particles is introduced into a drift tube with no electric field applied,

thereby avoiding losses associated with exposure of the particle sample to an adverse electric field. At the start of the transient separation, an electric field is applied that induces those particles located past a critical point to migrate toward the opposite end of the drift tube, where a large counterflow enters around the perimeter, and a smaller analyte flow exits at the center. The particle's mobility is inferred from its time-of-flight down the drift tube. This method relies on the availability of fast-response particle detectors that have recently become available.

Flagan (2004) proposed and modeled an alternate differential mobility classifier that has some features of that of Tammet (2003, 2011); like the DMA, this opposed migration aerosol classifier (OMAC) can continuously extract particles within a narrow range of mobilities for detection or use in other experiments. In this device, migration between two permeable electrodes that define the classification channel is opposed by a cross-flow (Q_{cf}) of particle-free gas through those electrodes. Particles, the electrical migration of which is balanced by the cross-flow, are advected between the porous electrodes by a smaller sample flow. The performance of the OMAC is similar to that of the DMA, except that the voltage at which diffusion *begins* to degrade resolution is much lower, and scales as $V \propto \mathcal{R}_{nd}$ (Downard et al. 2011) rather than as $V \propto \mathcal{R}_{nd}^2$ as in the DMA (Stolzenburg 1988; Flagan 1999). Because the length scale over which diffusion must act to affect resolution is the entire channel width, b, in the OMAC, but only $\sim \beta b$ in the DMA, the dynamic range of the OMAC can, in theory, be made much larger than that of *any* DMA of comparable resolving power and dimensions.

This article describes the design, simulation, and experimental characterization of a radial form of this new instrument. This Radial, Opposed-Migration, Ion and Aerosol Classifier (ROMIAC) enables measurement of ions and particles well into the low-nanometer regime, with resolution that has enabled mobility separation of peptide stereoisomers (Mui et al. 2013). Here, we describe the use of three-dimensional finite element simulations in modeling the performance of an instrument capable of probing a wide range ($\sim$ 600 $\times$) of mobilities (1 to 20 nm in diameter) at select fixed flow rates, and with $\mathcal{R}$ as high as ~20. We also report on the experimental validation of two nearly identical prototypes of the ROMIAC. Finally, we demonstrate that computational modeling is required to explain behavior that idealized models do not capture. We note that the development of the ROMIAC involved several iterations of design and simulation to attain the performance of the final design that we report below.

2. Instrument design

2.1. Desired features

Flagan (2004) described the OMAC concept in terms of a simple, rectilinear classification channel similar to that used in the first DMA (Erikson 1921; Flagan 1998). Most DMAs have, however, employed a cylindrical, axisymmetric geometry that eliminates the edge effects of the side walls in a rectilinear design. While a cylindrical OMAC could be built, producing cylindrical electrodes that are uniformly porous over their entire areas would be a technical challenge.

The RDMA (Zhang et al. 1995) attains the simplicity of planar electrodes, while eliminating the edge effects. Early unpublished prototypes of rectilinear OMACs yielded lower than predicted resolution, possibly the result of edge effects. In this study, we have, therefore, undertaken the design and development of a radial-flow OMAC. This instrument ultimately has important applications for molecular separations as well as for aerosols; it was first applied to molecular ion classification, including the separation of peptide stereoisomers (Mui et al. 2013). Hence, it has been labeled the radial opposed migration ion and aerosol classifier (ROMIAC).

Introducing the aerosol through the ground electrode, and extracting the particles through the same ground electrode eliminates the adverse potential gradient drawback common to DMAs, and, thereby, potentially enhances particle transmission relative to designs with an adverse potential gradient. A consequence of this design is that both the flow and electric field in the classification region deviate from the ideal ones considered in the initial conceptual models (Flagan 2004; Downard et al. 2011). The classified-aerosol outlet port is located at the center of the grounded screen electrode. Although the classified aerosol could exit through an open port through that electrode, that would distort the electric field. Instead, the classified aerosol outlet port in the present design rests directly on the grounded electrode screen, thereby maintaining a uniform electric field throughout the classification region at the potential expense of losses from diffusive deposition.

Uniform distribution of aerosol flow across the width (in the case of a rectilinear classifier) or around the introduction radius (in the case of cylindrical or radial classifiers) is essential if high resolution is to be attained. Aerosols are usually introduced into and extracted from classifiers via small (e.g., 6 mm, or 1/4 inch) tubing. The relatively high velocity flow in the sample introduction port must transition into a uniform flow around the perimeter of a radial flow instrument, or across the width of a rectilinear one. For radial classifiers, reasonably uniform distribution of incoming aerosol can be achieved by introducing the aerosol tangentially into a circular "racetrack" around the outer radius of the classifier, as in the cylindrical Vienna DMA

(Winklmayr et al. 1991) and the radial DMAs (Zhang et al. 1995; Brunelli et al. 2009), provided adequate pressure drop is maintained between the racetrack and the classification region.

2.2. Idealized design model

Transmission of a particle through any mobility classifier is governed by the balance of opposed drag and electric forces, $\mathbf{F}_D$ and $\mathbf{F}_E$, respectively (Figure 1a). Unlike a DMA in which the particles must migrate across a sheath flow that enters parallel to the aerosol flow, the cross-flow in the ROMIAC is introduced orthogonally to the electrodes and aerosol flow, so the fluid streamlines are inclined relative to the electric field lines (Figures 1b and c). The axial component of the fluid velocity (which is, nominally, the cross-flow velocity, u_{cf}) must balance the electrical migration velocity, v_{mig}, for a particle to remain within the classification channel; the smaller, radial component of the fluid velocity (which is, nominally, the aerosol flow velocity, u_a) transports particles from the sample inlet to the outlet.

In a ROMIAC configured such that aerosol enters the region between two parallel disk-shaped electrodes at the outer radius and classified aerosol is extracted from an outlet at the center of one of the electrodes, the relationship between the migration and cross-flow velocity for an idealized instrument in which the aerosol flow is initially uniformly distributed across the classification channel is

$$v_{mig} = EZ^* = \frac{Q_{cf}}{\pi\left(R_{elec}^2 - R_o^2\right)}, \qquad [10]$$

where $E = \nabla V \approx V/b$ is the electric field strength, b is the electrode separation distance, and R_{elec} and R_o are the electrode and outlet radii of the classifier, respectively. The ROMIAC deviates from this simplistic model in that the aerosol enters through the grounded electrode, as illustrated in Figure 2, which identifies key dimensions of the ROMIAC and illustrates characteristic trajectories of particles of different mobilities.

2.3. Design criteria and prototype specifications

The initial objective in the design of the ROMIAC was to enable particle size distribution measurements with constant resolution from 1 to 20 nm in diameter. The instrument flow rates were chosen to be compatible with existing condensation particle counters or electrometers that would be used to detect the classified particles. Hence, the aerosol and classified sample flow rates were initially constrained to be $Q_a = Q_c \approx 1$ lpm. Additionally, the ROMIAC was designed to classify sub-20 nm aerosol using pumps that were of modest weight and power consumption for airborne measurements, thus constraining $Q_{cf} < 50$ lpm. To enable measurements over a wide range of mobilities with minimal variation in $\mathcal{R}$, an electrode spacing of $b = 10$ mm was selected for the nominal design, allowing for a maximum voltage of ~10 kV (since particle diffusion effects are minimized at high voltages), though the prototype was designed with the flexibility to allow measurements to be made with electrode spacings as small as 1 mm for operation at lower peak voltages.

The foregoing specifications formed the basis for the prototype design of the ROMIAC. The aerosol flows from a tube with inner radius $R_o = 2.4$ mm, i.e., standard 1/4 inch stainless steel tubing, into an electrically

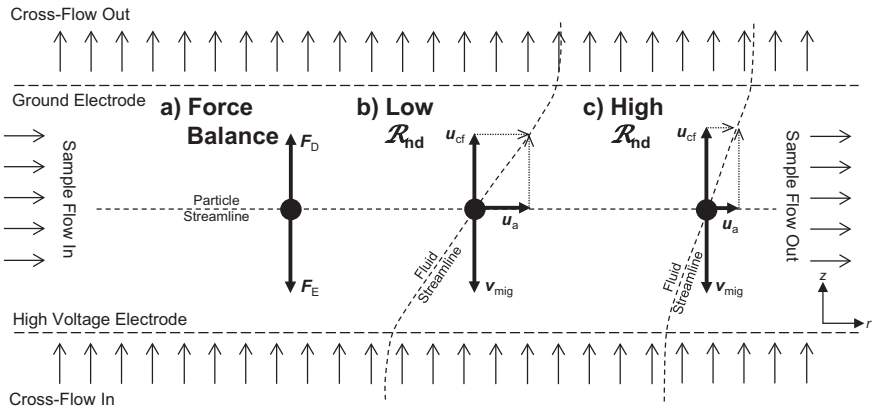

Figure 1. (a) Simplified diagram of balanced drag, $\mathbf{F}_D$, and electric, $\mathbf{F}_E$, forces acting on a particle of mobility Z^* in the ROMIAC classification region, resulting in a particle streamline that is parallel to the sample flow direction. (b) Simplified diagram of aerosol and cross-flow fluid velocities (u_a and u_{cf}, respectively) and electrical migration velocity, v_{mig}, acting on a particle of mobility Z^*. Low $\mathcal{R}_{nd}$ operation results in fluid streamlines that significantly deviate from vertical. Particles of mobility Z^* will thus experience a high advective velocity (relative to the cross-flow velocity) from sample inlet to outlet, increasing the transmission of all particles, and resulting in lower resolution. (c) High $\mathcal{R}_{nd}$ operation results in nearly vertical fluid streamlines, discriminating more heavily against the transmission of particles that are not of mobility Z^*.

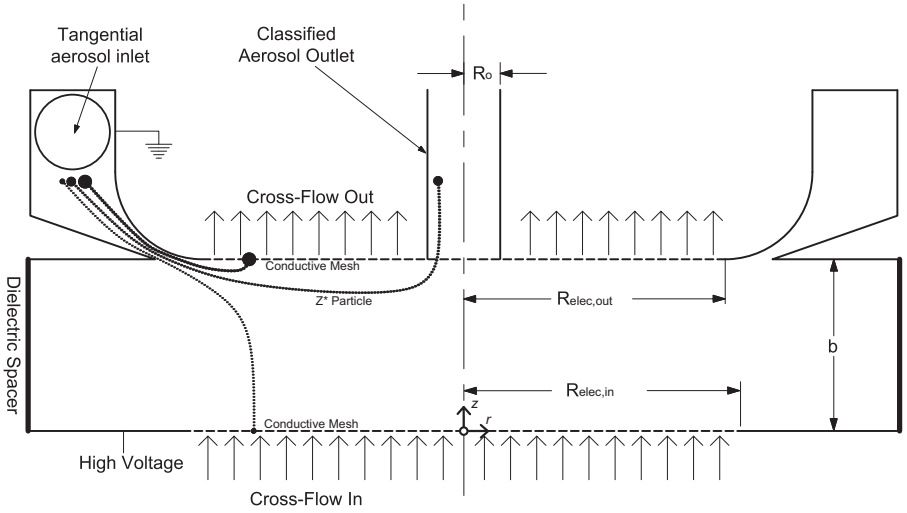

Figure 2. Schematic of ROMIAC aerosol introduction, classification region, and classified aerosol outlet. Particles are introduced via a tangential inlet tube to be azimuthally distributed through a thin knife-edge gap into the classification region, where particles follow characteristic trajectories based on the degree of balance of drag and electric forces experienced. Particles of mobility Z^* will be advected toward the center and extracted through the outlet. Key dimensions that define the classification region are indicated. The origin of the coordinate system is designated to be the center of the incoming cross-flow electrode.

grounded, tangential racetrack; the aerosol then passes through a narrow, azimuthal knife-edge gap to enter the classification region. In order to achieve the pressure drop required to ensure uniform flow through the entire annular aerosol entrance slot, the gap between the knife edge and the rounded edge of the ground electrode needs to be small. In the prototype ROMIAC, this gap can be adjusted by the insertion of precision shims, each of thickness $\Delta b_{\text{shim}} = 0.381$ mm, for the instrument reported here. The inter-electrode gap, b_{nom}, was defined by a 10 mm thick Delrin spacer. The cross-flow enters the ROMIAC through a conductive stainless steel mesh of radius $R_{\text{elec,in}} = 16.1$ mm and exits through the same material of radius $R_{\text{elec,out}} = 15.2$ mm. Mechanical design considerations constrain the outlet electrode mesh to have a slightly smaller radius than the entrance slot, and, therefore, the inlet electrode mesh (Figure 2). The classified sample outlet port is located at the center of the outlet grounded electrode, with inner radius $R_o = 2.4$ mm. Figure 3 shows the realized design of the ROMIAC, which has overall exterior dimensions of 10.5 cm in height and 11.4 cm in diameter. The two prototypes

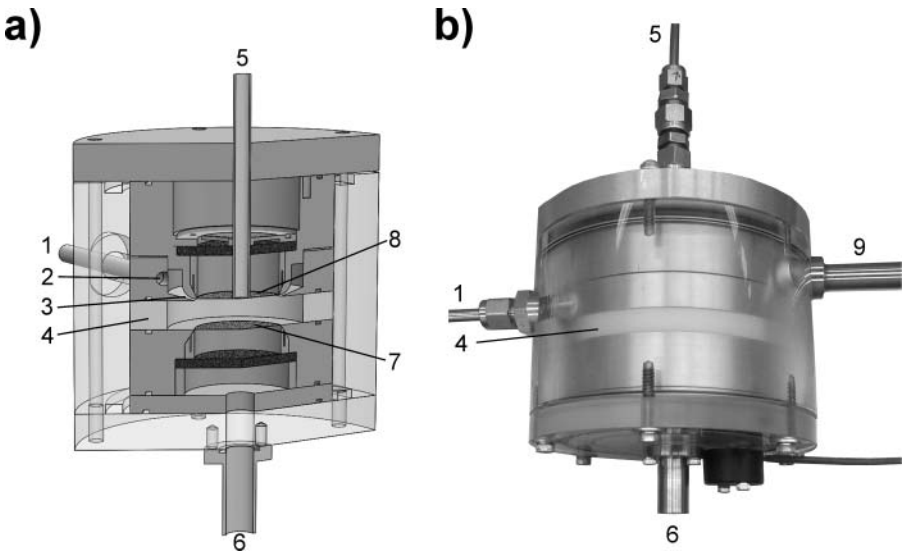

Figure 3. (a) Cutaway view and (b) photograph of ROMIAC with key features numbered. Overall exterior dimensions are 10.5 cm in height and 11.4 cm in diameter. (1) Aerosol inlet tube; (2) tangential inlet to distribution racetrack; (3) distribution knife-edge; (4) dielectric spacer; (5) classified aerosol outlet tube; (6) incoming cross-flow port; (7) high voltage porous electrode; (8) electrically grounded porous electrode; (9) outgoing cross-flow port.

used in this study are deemed "nearly identical" because they share identical dimensions and components, with the exception of the electrode meshes. The mesh used in one ROMIAC ("ROMIAC1") was 325-mesh (30% open area) while the mesh used in the other ROMIAC ("ROMIAC2") was 200-mesh (34% open area). Preliminary measurements were conducted in which ROMIAC1 had either 325-mesh or 200-mesh electrodes, with little difference in transmission efficiency observed; these measurements were also conducted with ROMIAC1 with 500-mesh (25% open area) electrodes, both without and with a hole cut in the outlet electrode (so that particles would not pass through a screen to exit through the outlet port), which also showed little difference in transmission efficiency (see the online supplementary information). The residence time for particles in the ROMIAC is estimated at ~0.7 s based on an assumed Q_a = 1 lpm and the volumes of the tubing and classification region; measurements associated with, but not reported, in Mui et al. (2013) suggested that a coupled ROMIAC-mass spectrometer showed response times of $\lesssim$0.5 s for a step increase in signal.

3. Simulation methods

3.1. Three-dimensional finite element analysis

Preliminary simulations entailed solving the flow and electrical fields within the ROMIAC as a two-dimensional, axisymmetric model in COMSOL Multiphysics™. The fluid and electrostatic maps were then imported and interpolated within Matlab™ to provide fluid flow and electric field values at any arbitrary point in *r*-*z* space to drive particle dynamics equations and simulate Monte Carlo diffusive particle trajectories within the classification region. Brownian diffusion of particles was simulated with pseudorandom fluctuations in the *r*- and *z*-directions. Though computationally inexpensive, the two-dimensional models did not capture the effect of the tangential inlet and distribution racetrack on particle transmission. Particles had to be introduced in the region near the converging entrance upstream of the knife edge gap to enter the classification region, due to the inaccurate representation of the inlet region in two-dimensional space.

Preliminary three-dimensional models in COMSOL Multiphysics™ using a rectangular coordinate system represented the effect of the tangential inlet and distribution racetrack more accurately, and employed the charged-particle tracing feature of the software. However, the need to account for Brownian diffusion rendered early models too computationally expensive and impractical. An improved three-dimensional model in COMSOL Multiphysics™ was developed in which the particles were modeled as "large ions" by solving the convective diffusion equation, thereby capturing the effect of Brownian diffusion with only slightly more computational expense than earlier two-dimensional models. Only the three-dimensional convective diffusion equation model will be discussed for the remainder of this study.

The model geometry was created to reflect the interior volumes in which the ions or particles are classified. These volumes include the full length of inlet tubing, the tangential introduction, the distribution racetrack, the distribution knife-edge gap, the classification region, and the full length of outlet tubing. The geometry included the effects of design compromises that were required to facilitate fabrication and assembly of the instrument. These compromises resulted in the electrode mesh not being perfectly aligned with the intended electrode plane, causing the electrode separation distance to be greater than the sum of b_{nom} = 10 mm and Δb_{shim} = 0.381 mm. The additional distance due to imperfect alignment of the electrode plane and the mesh was estimated from a fully assembled three-dimensional model of the ROMIAC in Solidworks™ (Figure 3a) as Δb_{mesh} = 0.94 mm, leading to a total electrode gap separation distance of $b_{total} = b_{nom} + \Delta b_{shim} + \Delta b_{mesh}$ = 11.32 mm.

The flow in the ROMIAC was modeled in the COMSOL Multiphysics™ fluid-flow module, assuming laminar, single-phase flow of a compressible fluid (air at 298 K) by solving the Navier–Stokes equations. Compressible flow was considered to allow substantial pressure drops to be simulated, though the pressure drops in the final design are sufficiently small that gas density variations are insignificant. Walls were assigned a no-slip boundary condition. The incoming aerosol boundary was located at the beginning of the inlet tube, with an assumed, atmospheric-pressure boundary condition. The classified aerosol outlet boundary was likewise located at the end of the outlet tube, with an assumed normal outflow velocity boundary condition of $Q_a/(\pi R_o^2)$. The porous electrodes served as the boundaries for the cross-flows, assuming a normal inflow and outflow velocity condition of $Q_{cf}/(\pi R_{elec,in}^2)$ and $Q_{cf}/[\pi(R_{elec,out}^2 - R_o^2)]$, respectively.

The electrostatics module was used to solve the Poisson equation for the electric fields. The Delrin electrode spacer (b_{nom} = 10 mm), which is the only dielectric component in the classification region, was assigned a zero charge boundary condition. All boundaries on the outgoing cross-flow side of the Delrin spacer were assigned a ground boundary condition (V = 0), while all boundaries on the incoming cross-flow side of the Delrin spacer were assigned an imposed electric potential boundary condition.

Particle concentrations in most atmospheric aerosol studies are low enough to qualify as a dilute species. The chemical species transport module was used to solve for the transport of dilute species by diffusion using Fick's law, convection using the fluid-flow solution, and migration using the electric-field solution. All boundaries, except for the aerosol inlet and outlet, were assigned a zero concentration boundary condition, which assumes that all particles will be lost upon contact with a wall. The aerosol inlet boundary was assigned a particle number concentration condition of $12 \times 10^3\,\mathrm{cm}^{-3}$; equivalently, a molar concentration condition of $2 \times 10^{-14}\,\mathrm{mol} \cdot \mathrm{m}^{-3}$ was supplied to COMSOL Multiphysics™. Compared to the electric field, space charge effects are negligible at this concentration. Positive, singly-charged particles were simulated as "large ions" via their particle diffusivities, $\mathcal{D} = ZkT/e$, where k is the Boltzmann constant, T is the temperature, and e is the elementary charge.

For a given set of flow rates, the fluid flow field and a unity-scaled electric field were solved once. For a given D_Z, a parametric voltage sweep followed, solving for the steady-state particle concentration solution at each voltage. The average concentrations at the ROMIAC inlet and outlet boundaries, $\overline{c}_{\mathrm{in}}$ and $\overline{c}_{\mathrm{out}}$ respectively, were calculated as the ratio of the velocity-weighted particle number flux to the fluid volumetric flux:

$$\overline{c} = \frac{\int_0^{R_o} [2\pi r |u_z(r)| c(r)]\mathrm{d}r}{Q_a}, \qquad [11]$$

where c is the particle number concentration, R_o can be the aerosol inlet or outlet radius, the r coordinate is local to the inlet or outlet, and the z coordinate is oriented to the inlet or outlet tube axis.

3.2. Simulation data inversion

Downard et al. (2011) derived a transfer function for a rectilinear OMAC by solving the convective-diffusive equation in Cartesian coordinates. Though this transfer function has the advantage of accounting for particle losses, it is difficult to use for data-fitting due to convergence issues. For a given $\mathcal{R}_{\mathrm{nd}}$ operating condition, this transfer function converges below voltages less than those usually probed experimentally.

Following the flux coordinate method of Stolzenburg (1988) with a shear-flow approximation to the OMAC velocity profile in a rectilinear OMAC (Flagan 2004), Mai (2016) demonstrated that the transfer function that Stolzenburg derived for the DMA (Stolzenburg 1988) is a reasonable approximation for the OMAC. The derivation and details of this transfer function are outside the scope of this study and will be the subject of a future publication. Hence, we apply the Stolzenburg transfer function to the OMAC for the present purposes. The probability that a particle of dimensionless mobility $\tilde{Z} = Z/Z^*$ is transmitted through the OMAC is fitted to the functional form:

$$\Omega(\tilde{Z}, \beta, \delta, \tilde{\sigma}) = \frac{\tilde{\sigma}}{\sqrt{2}\beta(1-\delta)}\left[\mathcal{E}\left(\frac{\tilde{Z} - (1+\beta)}{\sqrt{2}\,\tilde{\sigma}}\right) + \mathcal{E}\left(\frac{\tilde{Z} - (1-\beta)}{\sqrt{2}\,\tilde{\sigma}}\right) - \mathcal{E}\left(\frac{\tilde{Z} - (1+\delta\beta)}{\sqrt{2}\,\tilde{\sigma}}\right) - \mathcal{E}\left(\frac{\tilde{Z} - (1-\delta\beta)}{\sqrt{2}\,\tilde{\sigma}}\right)\right], \qquad [12]$$

where $\tilde{\sigma}^2 = G\tilde{Z}/(\mathcal{R}_{\mathrm{nd}}\mathrm{Pe}_{\mathrm{mig}})$ is the dimensionless measure of diffusional broadening, $\mathrm{Pe}_{\mathrm{mig}} = eVf/kT$ is the migration Péclet number (ratio of transport by electrophoretic migration to that by diffusion), f is a factor that accounts for nonuniformities in the electric field (unity in the case of radial classifiers), and $\mathcal{E}(y) = y\,\mathrm{erf}(y) + \pi^{-1/2}e^{-y^2}$. For simple shear flow, Mai (2016) found the geometry factor for the rectilinear OMAC to be

$$G = \begin{cases} \dfrac{8}{3}, & \xi = 0 \\ \dfrac{4\left\{\dfrac{4}{15}\left[\left(1-|\xi|^{5/2}\right) - (1-|\xi|)^{5/2}\right] + \dfrac{1}{3}\left(\dfrac{\xi}{\alpha}\right)^2\left[\left(1-|\xi|^{3/2}\right) - (1-|\xi|)^{3/2}\right]\right\}}{|\xi|(1-|\xi|)}, & 0 < |\xi| < 1 \\ 2\left[\dfrac{4}{3} + \left(\dfrac{1}{\alpha}\right)^2\right], & |\xi| \geq 1 \end{cases} \qquad [13]$$

where $\xi = \beta^{-1}\left(\tilde{Z} - 1\right) = \mathcal{R}_{\mathrm{nd}}(\tilde{Z} - 1)$ and $\alpha = L/b$ is the aspect ratio, where L is the electrode length. In the case of the ROMIAC, we use $L = R_{\mathrm{elec,avg}} - R_o$ to estimate G, where $R_{\mathrm{elec,avg}}$ is the average of $R_{\mathrm{elec,out}}$ and $R_{\mathrm{elec,in}}$.

Equation (12) captures the performance of the OMAC, but the specific parameter values must be

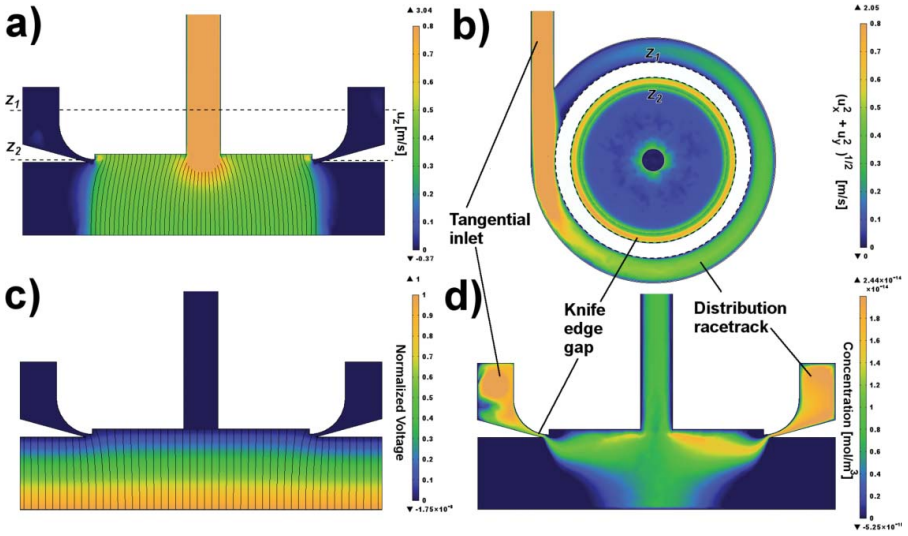

Figure 4. Example COMSOL Multiphysics™ solutions for the case of $Q_a/Q_{cf}/\mathcal{R}_{nd}/D_Z =$ 2 lpm/20 lpm/10/10 nm. Aerosol inlet and outlet tube extremities are cropped out of view. Color scales are restricted in range to distinguish areas of interest. Physical features of interest that may not be obvious are labeled. (a) Section view showing axial component of fluid flow velocity, u_z. Lines show fluid flow velocity streamlines that originate from the cross-flow inlet, and are truncated at the converging region near the aerosol outlet for clarity. Note that the vertical velocity increases approaching the centered aerosol outlet. Dashed lines z_1 and z_2 mark sections corresponding to those in (b). (b) Overhead view showing non-axial component of fluid flow velocity, $\sqrt{u_x^2 + u_y^2}$. Dashed circles z_1 and z_2 correspond to the cut planes in (a). The white ring between z_1 and z_2 indicates the absence of data, not zero velocity. Note that the non-vertical velocity increases approaching the centered aerosol outlet. (c) Section view showing the normalized electric potential solution. Lines show electric field lines that originate from the high voltage electrode surface. (d) Section view showing the particle concentration solution at a voltage corresponding to Z^*.

empirically determined to make the description quantitative. To this end, we introduce correction factors as has been done for the DMA (Stolzenburg 1988). Figure 4 shows an example of a COMSOL Multiphysics™ solution for the fluid flow, electric, and particle concentration fields. As seen in Figure 4, the fluid cross-flow velocity increases near the aerosol outlet radius, relative to the cross-flow velocity near the aerosol inlet radius. The magnitude of this effect varies with the flows through the instrument, so, for every pair of Q_a and Q_{cf}, there is a cross-flow velocity correction factor, $f_{u,z} = \overline{u}_{z,\mathrm{eff}}/\overline{u}_z$, where $\overline{u}_z = Q_{cf}/[\pi(R_{\mathrm{elec,out}}^2 - R_o^2 + R_{\mathrm{elec,in}}^2)/2]$ and $\overline{u}_{z,\mathrm{eff}}$ is the effective mean cross-flow velocity experienced by a particle of mobility Z^* following a typical (non-diffusive) trajectory through the ROMIAC classification region. To obtain an estimate of $\overline{u}_{z,\mathrm{eff}}$ from the COMSOL simulations, particles were initiated at the 50% point of the incoming aerosol flow velocity distribution across the knife-edge gap and allowed to change position in r-z space based on local flow and electric field conditions over constant 0.1 ms time steps. The applied voltage was such that the particle would be transmitted at the greatest efficiency, and the calculations were repeated until the particle reached the outgoing aerosol flow streamline corresponding to the 50% point of the outgoing aerosol flow velocity distribution across the aerosol outlet. The effective average vertical velocities reported are the azimuthally-averaged local u_z values stored for each particle location at every time step.

Furthermore, fabrication tolerances and the way the aerosol enters the classification region cause Z^* to deviate from that predicted from the V value used in the idealized, simplistic model in Equation (10). Thus, we introduce a mobility correction factor $f_Z = Z_{\mathrm{eff}}^*/Z^*$ to relate the effective peak particle mobility transmitted, Z_{eff}^*, to the classifier geometry and operating conditions, i.e.,

$$Z_{\mathrm{eff}}^* = f_Z Z^* = f_Z \left(\frac{Q_{cf}}{\pi\left(R_{\mathrm{elec,avg}}^2 - R_o^2\right)} \right) \left(\frac{b}{V} \right). \qquad [14]$$

The mobility correction factor for the present ROMIAC has three contributions:

(1) Reduced electric field strength from electric field distortions near the screen electrodes and/or possible modifications to the value of Δb_{mesh} in the assembled ROMIAC. These deviations from the simplistic model cause the observed Z^* to be higher than predicted by Equation (10). The effects of reduced field strength on transmitted mobility are described by a mobility correction factor, $f_{Z,E}$.

In the case of the COMSOL Multiphysics™ simulations, we assign a known value for Δb_{mesh} obtained from the Solidworks™ assembly, and the electric field is prescribed as though the permeable electrodes are solid, so $f_{Z,E} = 1$.

(2) The aerosol is introduced and extracted near the grounded electrode plane (between $z = b_{\mathrm{nom}}$ and $z = b_{\mathrm{nom}} + \Delta b_{\mathrm{shim}}$) rather than initially filling the space between the two electrodes (at $z = b_{\mathrm{total}}/2$), as might be assumed in deriving a simplistic model of the OMAC. Consequently, when the applied voltage is that calculated from Equation (10), the particles of mobility Z^* are advecting close to the grounded, cross-flow outlet electrode, enhancing diffusive particle losses. Therefore, the peak signal at the ROMIAC aerosol outlet will occur when the applied voltage is raised above the voltage suggested by the simplistic model, so as to move trajectories away from the cross-flow outlet electrode, and reduce losses.

(3) The effect of the central aerosol outlet on the vertical velocity that was described above.

We shall refer to the mobility correction factor due to reduced electric field strength (contribution 1) as $f_{Z,E}$ and the aerosol introduction and extraction bias (grouping contributions 2 and 3 together) as $f_{Z,\mathrm{bias}}$. Acknowledging all mobility correction contributions, we state that $f_Z = f_{Z,E} \times f_{Z,\mathrm{bias}}$.

The aerosol outlet flow direction being parallel to, and in the same direction as the cross-flow also implies that Q_c makes an additional contribution to Q_{cf} for resolving power purposes, at least for a portion of a particle's trajectory. The previous definition of non-diffusive resolution for the ROMIAC is a *nominal* value, $\mathcal{R}_{\mathrm{nd,nom}} = \left[\beta(1+|\delta|)\right]^{-1}$, from which we anticipate deviations. Hence, the ROMIAC data may, under some circumstances, show an apparent relative resolution $\mathcal{R}/\mathcal{R}_{\mathrm{nd,nom}} > 1$ due to the aforementioned flow bias. We introduce a flow-rate-ratio correction factor for the ROMIAC, defined as $f_\beta = \beta_{\mathrm{eff}}/\beta$, due to flow distortions in a small aspect ratio instrument. β_{eff} is the effective flow-rate ratio required to fit the data to Equation (12). Correspondingly, $\mathcal{R}_{\mathrm{nd,eff}} = \left[\beta_{\mathrm{eff}}(1+|\delta|)\right]^{-1}$ is the effective non-diffusive resolution limit for the ROMIAC.

DMAs do not generally attain the resolving power of an ideal instrument due to imperfections in the fabrication, flows, and electric fields; a correction factor for $\tilde{\sigma}$ has long been used to fit DMA data to transfer functions. Similarly, we define $f_{\tilde{\sigma}} = \tilde{\sigma}_{\mathrm{eff}}/\tilde{\sigma}$, where $\tilde{\sigma}_{\mathrm{eff}}$ is the effective diffusional broadening parameter that results in the best fit of the transfer function to the data. Incorporating the correction factors into Equation (12) yields the effective ROMIAC transfer function

$$\begin{aligned}\Omega_{\mathrm{eff}}(\tilde{Z}_{\mathrm{eff}}(f_Z),\beta,\delta,\tilde{\sigma},f_\beta,f_{\tilde{\sigma}}) &= \frac{\tilde{\sigma}f_{\tilde{\sigma}}}{\sqrt{2}\beta f_\beta(1-\delta)}\left[\mathcal{E}\left(\frac{\tilde{Z}_{\mathrm{eff}}-(1+\beta f_\beta)}{\sqrt{2}\tilde{\sigma}f_{\tilde{\sigma}}}\right)\right. \\ &+\mathcal{E}\left(\frac{\tilde{Z}_{\mathrm{eff}}-(1-\beta f_\beta)}{\sqrt{2}\tilde{\sigma}f_{\tilde{\sigma}}}\right)-\mathcal{E}\left(\frac{\tilde{Z}_{\mathrm{eff}}-(1+\delta\beta f_\beta)}{\sqrt{2}\tilde{\sigma}f_{\tilde{\sigma}}}\right) \\ &\left.-\mathcal{E}\left(\frac{\tilde{Z}_{\mathrm{eff}}-(1-\delta\beta f_\beta)}{\sqrt{2}\tilde{\sigma}f_{\tilde{\sigma}}}\right)\right], \end{aligned} \quad [15]$$

where $\tilde{Z}_{\mathrm{eff}} = Z/Z^*_{\mathrm{eff}} = Z/(f_Z Z^*)$ is the effective dimensionless mobility, and $\tilde{\sigma}$ is still calculated using $\mathcal{R}_{\mathrm{nd}}$, as defined above, rather than $\mathcal{R}_{\mathrm{nd,eff}}$.

The transfer function Ω_{eff} does not account for particle losses either in the classification region, or in the entrance and exit passages of the instrument. In the DMA, losses in the classification region are minor since particles are far from the walls for most of their transit; in the ROMIAC, particles are exposed to the classification channel's porous electrodes throughout their transit. We empirically characterize the combined effects of all of these loss mechanisms in the instrument efficiency, which is defined as the fraction of particles of mobility Z^* transmitted through the classifier, given its transfer function, i.e.,

$$\frac{\bar{c}_{\mathrm{out}}}{\bar{c}_{\mathrm{in}}} = \frac{\int\left[n_s(Z)\eta_{\mathrm{charge}}(Z)\Omega_{\mathrm{eff}}\left(\tilde{Z}_{\mathrm{eff}}(f_Z),\beta,\delta,\tilde{\sigma},f_\beta,f_{\tilde{\sigma}}\right)\eta_{\mathrm{trans}}(Z)\eta_{\mathrm{det}}(Z)\right]\mathrm{d}Z}{\int\left[n_s(Z)\eta_{\mathrm{charge}}(Z)\eta_{\mathrm{det}}(Z)\right]\mathrm{d}Z}, \quad [16]$$

where $n_s(Z)$ is the source aerosol size distribution, $\eta_{\mathrm{charge}}(Z)$ is the charging probability (unity in the simulations), $\eta_{\mathrm{trans}}(Z)$ is the classifier transmission efficiency, and $\eta_{\mathrm{det}}(Z)$ is the detector counting efficiency (unity in the simulations).

Inversion of the simulation data is fairly straightforward, as the source distribution is set as a single diameter in COMSOL Multiphysics™ and is, therefore, truly a Dirac delta function. Thus, the classifier transmission efficiency and transfer function are constant over the width of the source distribution and charging probability functions, and Equation (16) can be simplified to

$$\frac{\bar{c}_{\mathrm{out}}}{\bar{c}_{\mathrm{in}}} = \Omega_{\mathrm{eff}}\left(\tilde{Z}_{\mathrm{eff}}(f_Z),\beta,\delta,\tilde{\sigma},f_\beta,f_{\tilde{\sigma}}\right)\eta_{\mathrm{trans}}(Z). \quad [17]$$

Simulations were conducted over a wide range of flow rates for particle diameters ranging from 1 to 20 nm. Table 1 lists the flow rates and particle diameters for which simulations were conducted. For each simulation, the results were fitted to Equation (17) by finding values of $f_{Z,\mathrm{bias}}$ (since $f_{Z,E}$ is unity for the simulations), f_β, $f_{\tilde{\sigma}}$, and η_{trans} using the

Table 1. Nominal flow conditions and particle diameters for simulations and experiments in this study. Pe_{mig} and $Pe_{mig}\beta$ values are calculated for convenience in using Figures 7–9.

Q_a (lpm)	Q_{cf} (lpm)	$\mathcal{R}_{nd}$	β	$\frac{D_Z\ (nm)}{Pe_{mig}\|Pe_{mig}\beta}$						
2	13.3	6.7	0.15	$\frac{1.16^{SE}}{750\|110}$	$\frac{1.47^{SE}}{1.2e3\|180}$	$\frac{1.70^{SE}}{1.6e3\|240}$	$\frac{5^{SE}}{1.4e4\|1.2e3}$		$\frac{10^{SE}}{5.5e4\|8.2e3}$	$\frac{20^{SE}}{2.1e5\|3.2e4}$
2.5	13.3	5.3	0.19	$\frac{1.16^{SE}}{750\|140}$	$\frac{1.47^{SE}}{1.2e3\|230}$	$\frac{1.70^{SE}}{1.6e3\|310}$	$\frac{5^{SE}}{1.4e4\|2.6e3}$		$\frac{10^{SE}}{5.5e4\|1e4}$	$\frac{20^{SE}}{2.1e5\|4e4}$
3	13.3	4.4	0.23	$\frac{1.16^{SE}}{750\|170}$	$\frac{1.47^{SE}}{1.2e3\|280}$	$\frac{1.70^{SE}}{1.6e3\|370}$	$\frac{5^{SE}}{1.4e4\|3.2e3}$		$\frac{10^{SE}}{5.5e4\|1.3e4}$	$\frac{20^{SE}}{2.1e5\|4.9e4}$
2	16.6	8.3	0.12	$\frac{1.16^{SE}}{940\|110}$	$\frac{1.47^{SE}}{1.5e3\|180}$	$\frac{1.70^{SE}}{2e3\|240}$	$\frac{5^{SE}}{1.7e4\|2.1e3}$		$\frac{10^{SE}}{6.8e4\|8.2e3}$	$\frac{18^{SE}}{2.2e5\|2.6e4}$
2.5	16.6	6.6	0.15	$\frac{1.16^{SE}}{940\|140}$	$\frac{1.47^{SE}}{1.5e3\|230}$	$\frac{1.70^{SE}}{2e3\|300}$	$\frac{5^{SE}}{1.7e4\|2.6e3}$		$\frac{10^{SE}}{6.8e4\|1e4}$	$\frac{18^{SE}}{2.2e5\|3.2e4}$
3	16.6	5.5	0.18	$\frac{1.16^{SE}}{940\|170}$	$\frac{1.47^{SE}}{1.5e3\|270}$	$\frac{1.70^{SE}}{2e3\|360}$	$\frac{5^{SE}}{1.7e4\|3.1e3}$		$\frac{10^{SE}}{6.8e4\|1.2e4}$	$\frac{18^{SE}}{2.2e5\|3.9e4}$
2	20	10	0.10	$\frac{1.16^{SE}}{1.1e3\|110}$	$\frac{1.47^{SE}}{1.8e3\|180}$	$\frac{1.70^{SE}}{2.4e3\|240}$	$\frac{5^{SE}}{2.1e4\|2.1e3}$	$\frac{8^{E}}{5.3e4\|5.3e3}$	$\frac{10^{S}}{8.2e4\|8.2e3}$	$\frac{15^{SE}}{1.8e5\|1.8e4}$
2.5	20	8	0.13	$\frac{1.16^{SE}}{1.1e3\|150}$	$\frac{1.47^{SE}}{1.8e3\|240}$	$\frac{1.70^{SE}}{2.4e3\|320}$	$\frac{5^{SE}}{2.1e4\|2.7e3}$	$\frac{8^{E}}{5.3e4\|6.9e3}$	$\frac{10^{S}}{8.2e4\|1.1e4}$	$\frac{15^{SE}}{1.8e5\|2.4e4}$
3	20	6.7	0.15	$\frac{1.16^{SE}}{1.1e3\|170}$	$\frac{1.47^{SE}}{1.8e3\|270}$	$\frac{1.70^{SE}}{2.4e3\|360}$	$\frac{5^{SE}}{2.1e4\|3.1e3}$	$\frac{8^{E}}{5.3e4\|8e3}$	$\frac{10^{S}}{8.2e4\|1.2e4}$	$\frac{15^{SE}}{1.8e5\|2.7e4}$
2.1	13.9	6.6	0.15	$\frac{1.16^{SE}}{790\|120}$	$\frac{1.47^{SE}}{1.3e3\|190}$	$\frac{1.70^{SE}}{1.7e3\|250}$	$\frac{5^{SE}}{1.4e4\|2.2e3}$		$\frac{10^{SE}}{5.7e4\|8.6e3}$	$\frac{20^{SE}}{2.2e5\|3.3e4}$
2.25	20	8.9	0.11	$\frac{1.16^{SE}}{1.1e3\|120}$	$\frac{1.47^{SE}}{1.8e3\|200}$	$\frac{1.70^{SE}}{2.4e3\|270}$	$\frac{5^{SE}}{2.1e4\|2.3e3}$	$\frac{8^{E}}{5.3e4\|5.8e3}$	$\frac{10^{S}}{8.2e4\|9e3}$	$\frac{15^{SE}}{1.8e5\|2e4}$
2	30	15	0.07	$\frac{1.16^{S}}{1.7e3\|120}$	$\frac{1.47^{SE}}{2.7e3\|190}$	$\frac{1.70^{SE}}{3.6e3\|260}$	$\frac{5^{SE}}{3.1e4\|2.2e3}$		$\frac{10^{SE}}{1.2e5\|8.6e3}$	$\frac{12^{SE}}{1.8e5\|1.2e4}$
1.7	34.3	20.2	0.05	$\frac{1.16^{S}}{1.9e3\|100}$	$\frac{1.47^{SE}}{3.1e3\|160}$	$\frac{1.70^{SE}}{4.1e3\|210}$	$\frac{5^{S}}{3.6e4\|1.8e3}$		$\frac{10^{S}}{1.4e5\|7.1e3}$	$\frac{12^{S}}{2e5\|1e4}$

[S]COMSOL Multiphysics™ simulation conducted for this D_Z.
[E]Tandem-ROMIAC experiment conducted for this D_Z. (Electrosprayed molecular standards for $D_Z < 2$ nm and atomized NaCl for $D_Z \geq 5$ nm.)

Matlab™ nonlinear least-square solver ("lsqcurvefit" function) with multiple local minima optimization.

4. Experimental methods

4.1. Tandem-ROMIAC calibrations

Two nearly identical ROMIAC classifiers were constructed, ROMIAC1 and ROMIAC2. Tandem-ROMIAC measurements were performed with ROMIAC1 serving as the source classifier and ROMIAC2 serving as the test classifier (and vice versa, to compare the two nearly identical classifiers). Experiments were conducted using the same set of flow rates and particle diameters, so that the simulated and experimental performance could be compared. Each transmission measurement was repeated at least three times.

The first type of tandem-ROMIAC experiment probes the performance for sub-2 nm particles, using the experimental system shown in Figure 5a. Molecular standards were generated by electrospray ionization of tetra-alkyl ammonium halide (TAAX) solutions without use of an aerosol neutralizer. This study used 25 μM to 1 mM solutions of tetra-propyl ammonium iodide (TPAI), tetra-heptyl ammonium bromide (THAB), or tetra-dodecyl ammonium bromide (TDDAB) in methanol. The electrosprayed ions were classified by the source ROMIAC operated at a constant voltage with $Q_a/Q_{cf}/\mathcal{R}_{nd} = 2.1$ lpm/13.9 lpm/6.6, and then initially sent to a TSI 3068 electrometer to obtain a steady-state reference concentration. The classified aerosol flow was then directed to the test ROMIAC, which was stepped through voltages, before being detected by the electrometer to obtain a mobility distribution. The classified aerosol was then again sent directly to the electrometer to obtain a confirmatory steady-state reference concentration. Only the monomers of TPAI, THAB, and TDDAB were used as the molecular standards, since the classifier could unambiguously and completely differentiate these ions from other species without requiring the use of a mass spectrometer. The mobility diameters of the TPAI, THAB, and TDDAB monomers are 1.16, 1.47, and 1.7 nm, respectively (Ude and de la Mora 2005).

The second type of tandem-ROMIAC experiment probes the performance for particles from 5 to 20 nm, using the experimental system depicted in Figure 5b. A 0.2% by weight NaCl solution was atomized to produce an aerosol that was then sent through a Nafion dryer and a ^{85}Kr neutralizer. The source and test classifiers were operated at the same flow rates so the same transfer function *form* could be applied to both instruments during data inversion. As in the TAAX-ion experiments, the

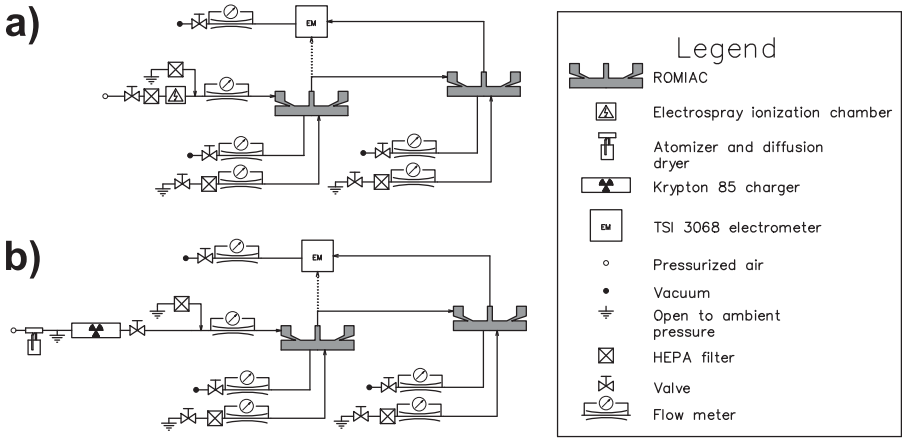

Figure 5. Experimental setup diagrams for tandem-ROMIAC measurements. (a) Electrosprayed TAAX molecular standards calibration. (b) Atomized NaCl calibration.

aerosol was initially transmitted through the source classifier at a fixed voltage directly to the electrometer to obtain a steady-state reference concentration; it was then directed through the test classifier, stepping through voltages to obtain a mobility distribution; the classified aerosol concentration was monitored using the electrometer. At the end of each measurement, the source aerosol reference concentration measurement was repeated. Because the distribution coming from the source aerosol is not truly monodisperse, the mobility distribution of the aerosol coming from the atomizer must be obtained for proper data inversion. After each tandem atomized NaCl measurement, the source classifier was also stepped through voltages and transmitted aerosol directly to the electrometer to obtain the atomizer output mobility distribution.

For both types of experiments, the ROMIAC cross-flows were operated as an open loop, with the incoming cross-flow coming from HEPA-filtered ambient air and the outgoing cross-flow produced by a vacuum pump. Laboratory ambient air temperature and relative humidity were about 24°C and 15%, respectively. Pressurized clean, dry air was used as the carrier gas for the electrospray ionization chamber and atomizer. Aerosol flow rates were measured by monitoring the flow rate through laminar flow elements using differential pressure transducers (Dwyer 607-4), while cross-flow rates were measured using thermal mass flow meters (TSI 201130 and 40241). Tubing lengths connecting the source and test classifiers to the electrometer were matched so that equivalent diffusive losses would occur when measuring the signal from either ROMIAC. Electrosprayed TAAX experiments used EMCO High Voltage CA12N power supplies, while atomized NaCl experiments used Bertan 602C-100N power supplies, to provide the ROMIAC applied voltages. Custom LabView^{TM} software was used for data acquisition and applied voltage control. A summary of all the experiments, along with nominal flow rates and particle diameter range, is presented in Table 1.

4.2. Experimental data inversion

The electrosprayed TAAX calibrations were performed such that the aerosol from the source classifier was a completely resolved TPAI, THAB, or TDDAB monomer, thus making the aerosol truly monodisperse from the perspective of the test classifier. This simplifies the inversion to the case of the simulation data, since the classifier transmission efficiency and transfer function (as well as charging probability) are constant over the width of the source distribution. The electrometer is assumed to have unity detection efficiency. A distinction in the case of inverting the electrosprayed TAAX data is that Δb_{mesh} is not known, and therefore, $f_{Z,E}$ cannot be assumed to be unity. We assume that the simulation values of $f_{Z,\mathrm{bias}}$ hold true for the experimental measurements for the same flow rates and particle diameters. Thus the results were fitted to Equation (17) by finding values of $f_{Z,E} = (b_{\mathrm{nom}} + \Delta b_{\mathrm{shim}} + \Delta b_{\mathrm{mesh}})/b_{\mathrm{nom}}$, f_{β}, $f_{\tilde{\sigma}}$, and η_{trans} (and assuming $f_{Z,\mathrm{bias}}$ from the simulations) in the same manner as the simulation data.

Inversion of the atomized NaCl data is more complex since the aerosol from the source classifier is not monodisperse. Tandem ROMIAC experiments using two, nearly identical classifiers were operated at the same flow rates, under the assumption that their transfer function *forms* are the same. For these data, we follow the approach used by Stolzenburg (1988) (see also Zhang and Flagan 1996; Hagwood et al. 1999) for inversion of tandem classifier data. Briefly, the particle concentration from the atomizer measured by the source (first)

classifier stepping through voltages V_1 is

$$\bar{c}_{\mathrm{out1}}(V_1) = \int \left[n_{\mathrm{eff}}(Z)\Omega_{\mathrm{eff1}}\left(\tilde{Z}_{\mathrm{eff1}}(f_{Z1}), \beta, \delta, \tilde{\sigma}, f_{\beta 1}, f_{\tilde{\sigma}1}\right)\right] \mathrm{d}Z, \quad [18]$$

where $n_{\mathrm{eff}}(Z) = n_{\mathrm{s}}(Z)\eta_{\mathrm{charge}}(Z)\eta_{\mathrm{trans1}}(Z)\eta_{\mathrm{det}}(Z)$ is the effective source distribution. Because the particle size range being probed is limited to the low nanometer regime, and the charge distribution is the same for both classifiers, we did not have to contend with multiply-charged particles or with the charge distribution for these calibration measurements. Quantification of the individual components of $n_{\mathrm{eff}}(Z)$ is unnecessary. The $f_{Z,E1}$ correction factor for the source classifier come from the averaged $f_{Z,E}$ values for that classifier from the electrosprayed TAAX experiments, while $f_{Z,\mathrm{bias1}}$, $f_{\beta 1}$, and $f_{\tilde{\sigma}1}$ are from the simulations for the same flow rates and particle diameters, since the relationships for these factors derived from the sub-2 nm TAAX experiments should not be extrapolated for the $D_Z = 5$ to 20 nm size range. The $n_{\mathrm{eff}}(Z)$ is assumed to be well-represented by a log normal distribution with three parameters found by fitting to the measured atomizer distribution. With a functional approximation of $n_{\mathrm{eff}}(Z)$, the particle concentration from the test (second) classifier, stepping through voltages V_2, of the aerosol coming from the source classifier at fixed V_1 can be used to solve for $f_{Z2}, f_{\beta 2}, f_{\tilde{\sigma}2}$, and η_{trans2}:

$$\frac{\bar{c}_{\mathrm{out2}}(V_1, V_2)}{\bar{c}_{\mathrm{in2}}(V_1)} = \frac{\bar{c}_{\mathrm{out2}}(V_1, V_2)}{\bar{c}_{\mathrm{out1}}(V_1)} = \frac{\int \left[n_{\mathrm{eff}}(Z)\Omega_{\mathrm{eff1}}\left(\tilde{Z}_{\mathrm{eff1}}(f_{Z1}), \beta, \delta, \tilde{\sigma}, f_{\beta 1}, f_{\tilde{\sigma}1}\right)\Omega_{\mathrm{eff2}}\left(\tilde{Z}_{\mathrm{eff2}}(f_{Z2}), \beta, \delta, \tilde{\sigma}, f_{\beta 2}, f_{\tilde{\sigma}2}\right)\eta_{\mathrm{trans2}}(Z)\right] \mathrm{d}Z}{\int \left[n_{\mathrm{eff}}(Z)\Omega_{\mathrm{eff1}}\left(\tilde{Z}_{\mathrm{eff1}}(f_{Z1}), \beta, \delta, \tilde{\sigma}, f_{\beta 1}, f_{\tilde{\sigma}1}\right)\right] \mathrm{d}Z}, \quad [19]$$

where $f_{Z,E2}$ for the test classifier can be calculated by dividing the best-fit f_{Z2} by the simulation-estimated $f_{Z,\mathrm{bias2}}$ for the same flow rates and particle diameters.

5. Results and discussion

The simulations and experiments combine to produce data from which the fraction of particles of a given size or mobility that are transmitted through the instrument can be deduced by the aforementioned methods. Figure 6 shows representative plots of this fraction, $c_{\mathrm{out}}/c_{\mathrm{in}}$. Figures 6a and b show the results obtained from simulations for relatively low operating resolution classification of small particles, i.e., $\mathcal{R}_{\mathrm{nd,nom}} = 4.4$ and $D_Z = 1.47$ nm, and moderate operating resolution classification of larger particles, $\mathcal{R}_{\mathrm{nd,nom}} = 15$ and $D_Z = 12$ nm, respectively. The fit to the Stolzenburg transfer function in Equation (15) is also shown, and the fit parameters are given. Figures 6c and d each compare measured transmission fractions for the two ROMIACs for THAB ions ($D_Z = 1.47$ nm) at the same two flow rate conditions that were simulated. Figures 6e and f show tandem-ROMIAC data for large (10–12 nm) NaCl particles. In each case, the quality of the fit of the simulation or experimental data was high, suggesting that this representation of the transfer function is suitable for use in inverting the ROMIAC data (or OMAC in general), once the empirical correction factors are known. As noted in the simulation data inversion section, these correction factors address specific physical issues that cause the actual instrument to deviate from the simplistic model used to describe the instruments. Therefore, we discuss each of the mechanisms that requires correction in turn, and provide the quantitative descriptions of the correction factors in the discussion that follows.

5.1. Cross flow velocity nonuniformity

In the simplified, conceptual model of the OMAC or ROMIAC, the areas of the two porous electrodes are assumed to be identical, and the cross-flow velocity is assumed to be uniform throughout the classification region. Locating both the aerosol inlet and outlet ports in the grounded electrode enabled classification without forcing the particles to pass through an adverse potential gradient, but makes it impossible to achieve the uniformity of the idealized instrument.

Since the ROMIAC geometry precludes direct measurement of the gas velocity within the classification region, we employ the simulations to assess the impact and magnitude of this flow distortion. As seen in Figure 4a, the cross-flow velocity varies only slowly with radial and axial position within the classification region. The cross-flow velocity converges and accelerates as it approaches the grounded top electrode.

An estimate of $f_{u,z}$ was obtained by using COMSOL Multiphysics™ flow field solutions to derive Matlab™-calculated non-diffusive particle trajectory simulations, recording the azimuthally-averaged vertical velocity acting on the particles at each time step as they are transmitted through the ROMIAC. Figure 7a shows the dependence of $f_{u,z}$ on the nominal flow rate ratio β_{nom} (averaged for all D_Z for a given operating β listed in Table 1) from the COMSOL Multiphysics™-Matlab™ kinematic trajectory

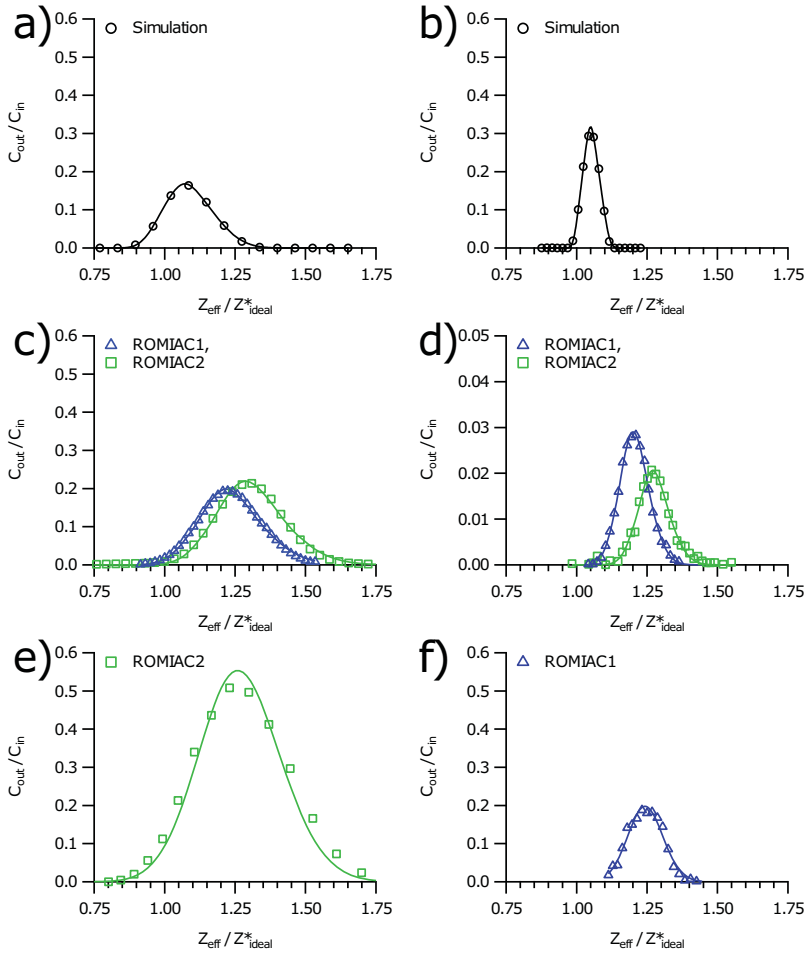

Subfigure	Classifier	$Q_{a,nom}$ [lpm]	$Q_{cf,nom}$ [lpm]	$\mathcal{R}_{nd,nom}$	$D_{Z,nom}$ [nm]	$f_{Z,bias}$	$f_{Z,E}$	f_β	σ^2_{distor}	η_{trans}	$\mathcal{R}/\mathcal{R}_{nd,eff}$
a	Simulation	3	13.3	4.4	1.47	1.06	1.00	0.71	9.E-04	0.20	0.82
b	Simulation	2	30	15	12	1.06	1.00	0.91	8.E-05	0.36	0.84
c	ROMIAC1	3	13.3	4.4	1.47	1.07	1.14	0.53	5.E-03	0.34	0.56
c	ROMIAC2	3	13.3	4.4	1.47	1.07	1.20	0.60	2.E-03	0.34	0.62
d	ROMIAC1	2	30	15	1.47	1.05	1.14	1.00	7.E-04	0.04	0.70
d	ROMIAC2	2	30	15	1.47	1.05	1.21	0.89	5.E-04	0.04	0.65
e	ROMIAC2	3	13.3	4.4	10	1.07	1.17	0.71	2.E-03	0.94	0.49
f	ROMIAC1	2	30	15	12	1.05	1.17	1.00	9.E-04	0.35	0.53

Figure 6. Example measurements (points) and transfer function fits (lines) with listed operating conditions and fitting parameters. Top row: COMSOL Multiphysics™ simulation examples for (a) small D_Z at low $\mathcal{R}_{nd,nom}$ operation and (b) large D_Z at high $\mathcal{R}_{nd,nom}$ operation. Middle row: tandem-ROMIAC TAAX measurement examples for (c) small D_Z at low $\mathcal{R}_{nd,nom}$ operation and (d) small D_Z at high $\mathcal{R}_{nd,nom}$ operation. Bottom row: tandem-ROMIAC NaCl measurement examples for (e) large D_Z at low $\mathcal{R}_{nd,nom}$ operation and (f) large D_Z at high $\mathcal{R}_{nd,nom}$ operation.

simulations. The linear relationship ($r^2 = 0.85$) is

$$f_{u,z} = 1.01 + 0.11\beta_{nom}. \quad [20]$$

The error in estimating $\overline{u}_z$ acting on particles during classification is related to flow distortions in the ROMIAC with increasing β_{nom}. Additionally, having a cross-flow outlet electrode of lesser area than the cross-flow inlet electrode would result in generally higher vertical velocities near the outlet electrode. Since the particles are introduced and extracted near the outlet electrode in this ROMIAC, the particles generally experience higher axial velocities than presumed in calculating $\overline{u}_z$ based upon simplistic geometry models.

Figure 7b shows the linear dependence of $f_{Z,bias}$ on $f_{u,z}$ and an additional dependence on the particle migration Péclet number, as indicated by the color banding. Acknowledging these dependencies, an empirical function of these two parameters to predict the mobility correction factor due to inlet/outlet bias is

$$f_{Z,bias} = 1.13 f_{u,z} + \frac{0.03}{\log_{10}(Pe_{mig})} - 0.11 \quad [21]$$

with $r^2 = 0.98$. The one-to-one comparison of the

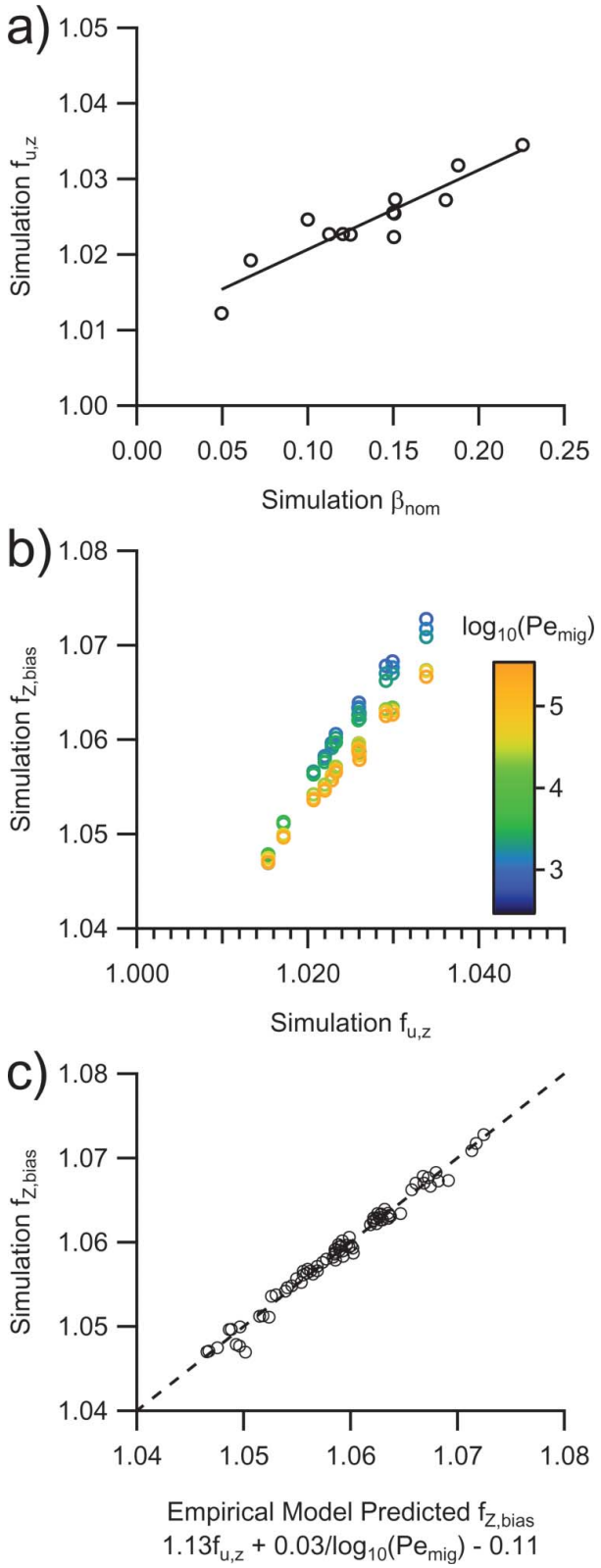

Figure 7. Simulation results used to estimate $f_{Z,bias}$. (a) $f_{u,z}$ (from COMSOL Multiphysics™-driven kinematic particle trajectories) against β_{nom}. Best-fit line is $f_{u,z} = 1.01 + 0.11\beta_{nom}$. (b) $f_{Z,bias}$ against estimated $f_{u,z}$ colored by Pe_{mig}. (c) 1-to-1 comparison of simulation $f_{Z,bias}$ against those estimated from an empirical function of $f_{u,z}$ and Pe_{mig}. For convenience, Pe_{mig} values are listed in Table 1.

simulation $f_{Z,bias}$ values to those predicted by Equation (21) is shown in Figure 7c.

5.2. Electric field strength reduction

Equation (21) was used to estimate the $f_{Z,bias}$ component of f_Z in fitting the tandem-ROMIAC TAAX experiments to Equation (17). Therefore, the remaining discrepancy between the nominal and a greater effective mobility is due to an additional electric field strength reduction beyond that resulting from an interelectrode spacing of $b_{nom} = 10$ mm, quantified as $f_{Z,E}$. For ROMIAC1 and ROMIAC2, their average mobility correction factors (with relative standard deviation) due to the electric field strength reduction were $f_{Z,E,ROMIAC1} = 1.14(\pm 4.5\%)$ and $f_{Z,E,ROMIAC2} = 1.17(\pm 3.9\%)$, respectively. Though it is possible that the value of Δb_{mesh} is greater than that estimated from the Solidworks™ assembled model, an additional explanation for the observed reduction in electric field strength is that the electric field may be distorted near the screen electrodes.

5.3. Flow rate ratio

The observed resolution of the ROMIAC is somewhat higher than predicted from the simple ratio of flow rates, i.e., $\mathcal{R} > \beta^{-1}$. As discussed above, the outgoing aerosol flow, Q_c, which exits through the same plane as the outgoing Q_{cf}, increases $\overline{u}_z$ (for a portion of the particle's trajectory) against which a particle must migrate in order to successfully reach the aerosol outlet. As a result, f_β should vary inversely with the vertical velocity $f_{u,z}$. Figures 6a–d indeed show that the fitted f_β values are higher for the cases where the operating resolutions are higher and the particles would not experience as much axial velocity enhancement (Figure 7a). However, Figures 6c,e and d,f also suggest that another factor, such as particle size, can influence f_β.

Figure 8a shows the inverse dependence of simulation f_β values on $f_{u,z}$ and Pe_{mig}. Acknowledging these dependencies, an empirical function of these two parameters to predict the simulation flow rate ratio correction factor is

$$f_\beta = \frac{18.4}{f_{u,z}} + \frac{0.6}{\log_{10}(Pe_{mig})} - 17.3 \qquad [22]$$

with $r^2 = 0.84$. The one-to-one comparison of the simulation f_β values to those predicted by Equation (22) is shown in Figure 8b. The comparison of the empirical function to experimental f_β values is shown in Figure 8c, demonstrating that the empirical model is able to predict many of the experimental values.

5.4. Diffusional broadening parameter

The parameter $\tilde{\sigma}$ accounts for the role that Brownian diffusion of particles plays in degrading the classification efficiency. Other factors that cause particles to deviate from their ideal trajectories through a classifier can lead to similar degradation that is empirically described through the value of $f_{\tilde{\sigma}}$. Examination of the flow in the aerosol introduction plenum (Figure 4b) reveals that the tangential velocity around this racetrack decreases dramatically from the tangential inlet. While the pressure drop through the knife-edge inlet is designed to be large enough to ensure uniform flow through that slot, some azimuthal variation in the flow rate must exist due to the pressure drop in the flow around the racetrack. Thus, particle losses may vary within this region, though this would only affect the transmission efficiency and not the resolution since this region precedes the classification region and can be regarded as extra tubing through which particles travel. Other factors may lead to particles along different trajectories experiencing different gas velocities or electric fields. $f_{\tilde{\sigma}}$ represents the apparent

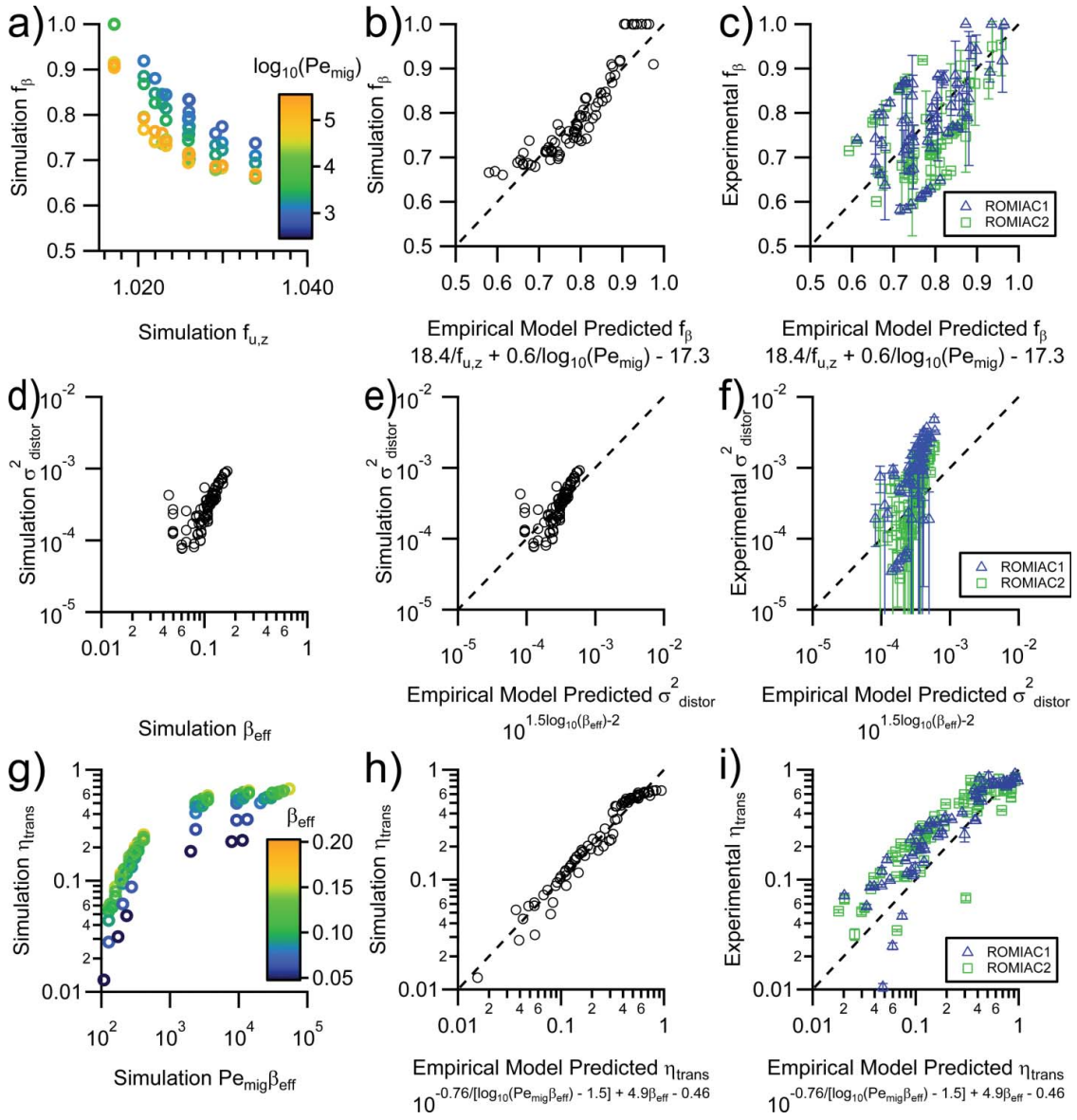

Figure 8. COMSOL Multiphysics™ simulation correction factor relationships, comparison of simulation values to empirical functions, and comparison of experimental values to empirical functions. Error bars in experimental results represent 2 standard deviations of multiple measurements. Top row: (a) simulation f_β against $f_{u,z}$ colored by Pe_{mig}. (b) 1-to-1 comparison of simulation f_β against empirical model of $f_{u,z}$ and Pe_{mig}. (c) 1-to-1 comparison of experiment-fitted f_β against empirical model of $f_{u,z}$ and Pe_{mig}. Middle row: (d) simulation $\tilde{\sigma}^2_{distor}$ against β_{eff}. (e) 1-to-1 comparison of simulation $\tilde{\sigma}^2_{distor}$ against empirical model of β_{eff}. (f) 1-to-1 comparison of experiment-fitted $\tilde{\sigma}^2_{distor}$ against empirical model of β_{eff}. Bottom row: (g) simulation η_{trans} against $Pe_{mig}\beta_{eff}$ colored by β_{eff}. (h) 1-to-1 comparison of simulation η_{trans} against empirical model of Pe_{mig} and β_{eff}. (i) 1-to-1 comparison of experiment-fitted η_{trans} against empirical model of Pe_{mig} and β_{eff}. For convenience, Pe_{mig} and $Pe_{mig}\beta$ values are listed in Table 1.

diffusivity enhancement of particles across classifier output mobility channels as a result of flow distortions owing to the real-instrument geometry.

This particle-size-independent dispersion contribution is modeled as an empirically determined additive term, $\tilde{\sigma}^2_{\text{distor}}$ (Stolzenburg 1988; Flagan 1999; Jiang et al. 2011), such that $\tilde{\sigma}^2_{\text{eff}} = \tilde{\sigma}^2 + \tilde{\sigma}^2_{\text{distor}} = (f_{\tilde{\sigma}}\tilde{\sigma})^2$. Solving for $\tilde{\sigma}^2_{\text{distor}}$ yields

$$\tilde{\sigma}^2_{\text{distor}} = \tilde{\sigma}^2\left(f^2_{\tilde{\sigma}} - 1\right). \quad [23]$$

Figure 8d shows the empirically derived dependence of $\tilde{\sigma}^2_{\text{distor}}$ on β_{eff}:

$$\tilde{\sigma}^2_{\text{distor}} = 10^{1.5\log_{10}(\beta_{\text{eff}}) - 2} \quad [24]$$

with $r^2 = 0.53$. The one-to-one comparison of the simulation $\tilde{\sigma}^2_{\text{distor}}$ values to those predicted by Equation (24) is shown in Figure 8e; experimental $\tilde{\sigma}^2_{\text{distor}}$ values show an even stronger dependence on β_{eff} (Figure 8f) than the simulation suggests.

5.5. Efficiency

Figure 8g shows the relationship between η_{trans} and $\text{Pe}_{\text{mig}}\beta_{\text{eff}}$, with an apparent additional dependence on β_{eff}. An empirical function to predict η_{trans} from Pe_{mig} and β_{eff} is

$$\eta_{\text{trans}} = 10^{-0.76/\left[\log_{10}\left(\text{Pe}_{\text{mig}}\beta_{\text{eff}}\right) - 1.5\right] + 4.9\beta_{\text{eff}} - 0.46}, \qquad \text{Pe}_{\text{mig}}\beta_{\text{eff}} \geq 10^{1.5} \quad [25]$$

with $r^2 = 0.96$, shown in Figure 8h. An asymptotic analysis of the transfer function for an idealized, rectilinear OMAC (Downard et al. 2011) supports the observed dependence of η_{trans} on β. The experimental η_{trans} values are compared with those predicted by Equation (25) in Figure 8i. Both classifiers tended to exhibit η_{trans} higher by a factor of 2 than either the simulations, or that predicted by Equation (25).

Two possible causes for this deviation are numerical diffusion in the simulations, or overestimation of the losses to the walls (the porous electrode surfaces could allow some particles to escape capture). Similar three-dimensional COMSOL Multiphysics™ models conducted for a high aspect ratio (length/electrode spacing ratio = 44) DMA showed deviations of $\leqslant$ 5% of the peak from the semi-analytical DMA transfer function of Stolzenburg (1988); this suggests that numerical diffusion plays a relatively minor role in the discrepancy between the ROMIAC simulation and experimental η_{trans} values, and that much of the deviation is due to the zero particle concentration boundary condition applied to the walls in the model that is overestimating particle losses. Nonetheless, the experimental results still appear to reflect the $\text{Pe}_{\text{mig}}\beta_{\text{eff}}$ dependence from the simulation-derived empirical function.

5.6. Resolution

Figure 9a shows the resolutions achieved by the ROMIAC (only $\mathcal{R}_{\text{nd,nom}} =$ 5.3, 10, and 20.2 are shown for clarity). For a given flow-rate-ratio and voltage in the diffusion-dominated regime, DMA-type classifiers suffer from greater degradation of resolution than OMAC-type classifiers. The simulation and experimental data show that in the diffusion-dominated regime, the ROMIAC generally achieves resolutions associated with the theoretical OMAC curves. The maximum observed resolution in Figure 9a was $\mathcal{R} \approx 18$ for TDDAB monomer classified by ROMIAC2.

The relative resolution $\mathcal{R}/\mathcal{R}_{\text{nd}}$ provided by a classifier cannot exceed unity, even in the non-diffusive regime. In the case of the ROMIAC, relative resolution can appear to exceed unity if $\mathcal{R}_{\text{nd,nom}}$ is used as the upper limit. Because Q_c contributes to the cross-flow for a portion of a particle's trajectory through the ROMIAC, the effective non-diffusive resolution $\mathcal{R}_{\text{nd,eff}}$ is used to estimate the relative resolution, as it accounts for the resolution enhancement from the aerosol outlet position and flow direction.

Figure 9b shows the effective relative resolution of the simulations and experiments for the ROMIAC against voltage and Pe_{mig}. The simulations achieve the highest $\mathcal{R}/\mathcal{R}_{\text{nd,eff}}$ values, reaching ~0.83 in the non-diffusive regime, though $\mathcal{R}/\mathcal{R}_{\text{nd,eff}}$ starts decreasing at $\text{Pe}_{\text{mig}} < 5 \times 10^3$. The experimental effective relative resolutions are comparable to the simulations at $\text{Pe}_{\text{mig}} < 5 \times 10^3$, but are lower than the simulation values for greater Pe_{mig} values, at ~0.65 in the non-diffusive regime. Like the diffusional broadening enhancement, degraded relative resolution can potentially be attributed to flow disturbances owing to non-ideal geometry and azimuthal flow asymmetry, just as such nonidealities degrade resolution in some DMAs. The results indicate that $\mathcal{R}/\mathcal{R}_{\text{nd,eff}}$ show little variation over about three orders of magnitude of V or Pe_{mig} for $4 < \mathcal{R}_{\text{nd,nom}} \leq 20$. $\mathcal{R}/\mathcal{R}_{\text{nd,eff}}$ did not deteriorate even as the voltage was reduced to that required to classify ~1 nm particles. This uniform relative resolution over a wide range of mobilities was possible since diffusion becomes important in an OMAC at roughly an order of magnitude lower V than in a DMA, as shown by the dashed and dotted lines in Figure 9.

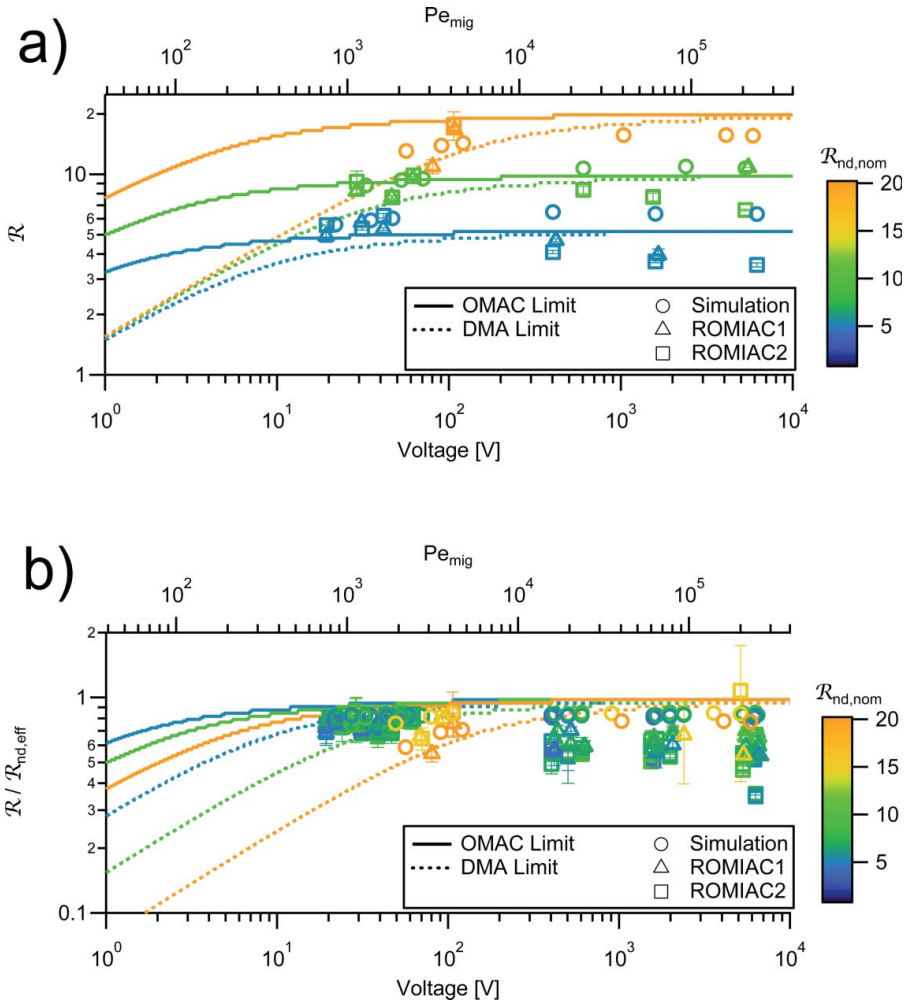

Figure 9. (a) Theoretical (lines) and observed simulation and experimental (markers) resolution obtained with the ROMIAC against V and $\mathrm{Pe_{mig}}$. Curves and markers for only three values of $\mathcal{R}_{\mathrm{nd,nom}}$ are displayed for clarity ($\mathcal{R}_{\mathrm{nd,nom}} =$ 5.3, 10, and 20.2). (b) Theoretical (lines) and observed simulation and experimental (markers) effective relative resolution obtained with the ROMIAC against V and $\mathrm{Pe_{mig}}$. Markers for all operating conditions are shown, but curves for only three values of $\mathcal{R}_{\mathrm{nd,nom}}$ are displayed for clarity ($\mathcal{R}_{\mathrm{nd,nom}} =$ 5.3, 10, and 20.2). Error bars in experimental results represent 1 standard deviation of multiple measurements. For convenience, $\mathrm{Pe_{mig}}$ values are listed in Table 1.

5.7. Comparison to other classifier studies

Table 2 lists the flow rates, resolutions, and particle diameters used in other cylindrical and radial classifier studies. The key dimensions of the ROMIAC are generally smaller than those of early radial DMAs such as the Spectrometre de Mobilite Electrique Circulaire (SMEC; Fissan et al. 1998) or that of Zhang et al. (1995) that probed larger particles, but larger than those of the nano-RDMA (Brunelli et al. 2009) that measures only particles in the lower portion of the ROMIAC measurement range. The f_Z factors of the ROMIAC are separated into contributions, while Zhang and Flagan (1996) present f_Z for the RDMA as a function of $\mathrm{Pe_{mig}}$ and the nano-RDMA presents an overall f_Z value. Values of $f_{Z,E}$ for the ROMIAC are comparable to that for the nano-RDMA f_Z value.

The effective length, L_{eff}, is a parameter that has been used in numerous studies of other instruments (e.g., Cheng 2001; Jiang et al. 2011) to represent inlet and outlet losses in terms of the equivalent length of straight tubing that would result in the same diffusive losses as the classifier. While this metric does not describe the actual instrument, it captures some of the flow-rate and particle size dependence of the particle losses within the instrument. The ROMIAC η_{trans} values did not, however, fit the Gormley-Kennedy diffusion model form as proposed for DMAs by Cheng (2001), as the ROMIAC η_{trans} values describe the total efficiency of the classifier (inlet, classification region, and outlet) and depend on β_{eff} in addition to Q_a. It is possible to fit the ROMIAC η_{trans} values to a Gormley-Kennedy diffusion model if it is assumed that the model represents the *extrinsic* transmission of particles (outside the classification region) while using a separate linear function of β_{eff}

Table 2. Geometry parameters, fitting factors, and typical flow conditions for various DMAs.

Cylindrical classifier	Inner radius (cm)	Outer radius (cm)	Channel length (cm)	f	f_Z	L_{eff} (m)	Q_a (lpm)	Q_{sh} (lpm)	$\mathcal{R}_{nd,nom}$	$\mathcal{R}/\mathcal{R}_{nd,nom}$	D_Z range (nm)	Source(s)
TSI-Long	0.937	1.958	44.44	0.707		7.1	1–3	5–20	4–20	0.5–1	8–1000	Fissan et al. (1996) Birmili et al. (1997) Flagan (1999)
TSI-Short	0.937	1.958	11.11	0.707			1	10	10	0.6–0.8	5–50	Fissan et al. (1996) Flagan (1999)
TSI-Nano	0.937	1.905	4.987	0.716		1.4, 2.24	1–1.5	7.5–30	10–30	0.3–1	1.16–50	Chen et al. (1998) Jiang et al. (2011)
Grimm nanoDMA	1.3	2	1.3	0.81		3.87	2	21.9	11	0.5–0.6	1.16–1.70	Jiang et al. (2011)
Vienna-Long	2.9	3.7	60	0.867		4.6	1–3	10–12	4–10	0.6–0.8	10–1000	Winklmayr et al. (1991) Birmili et al. (1997)
Vienna-Short	2.5	3.3	11	0.837		4.6	2–5	20–28	5.6–10	0.4–0.9	1–150	Winklmayr et al. (1991) Birmili et al. (1997) Karlsson and Martinsson (2003)
Karlsruhe-Vienna	2.29	3.3	2.5	0.838		11.53	6	61.4	10	0.5–0.7	1.16–1.70	Jiang et al. (2011)
Rosell-Llompart	2.5	3.3	1.6	0.867			1.45–3.6	10.78–202.2	7.4–56	0.17–0.31	1.12–1.90	Rosell-Llompart et al. (1996) Flagan (1999)
Radial classifier	**Inner radius (cm)**	**Outer radius (cm)**	**Gap thick-ness (cm)**	f	f_Z	L_{eff} (m)	Q_a (lpm)	Q_{sh} (lpm)	$\mathcal{R}_{nd,nom}$	$\mathcal{R}/\mathcal{R}_{nd,nom}$	D_Z range (nm)	Source(s)
SMEC	~0.5	6.5	0.4	1.0		16	1	10	10	0.4–1	6–50	Fissan et al. (1996)
Caltech RDMA	0.24	5.04	1.0	1.0	0.989–1.07	0.083–1.99	0.3–2	3–20	10	0.2–0.79	1.16–200	Zhang et al. 1995 Zhang and Flagan (1996) Birmili et al. (1997) Jiang et al. (2011)
Caltech nano-RDMA	0.24	0.75	1.0	1.0	1.15	0.87	0.6–1.5	6–15	10–17	0.3–0.6	1.16–1.8	Brunelli et al. (2009) Jiang et al. (2011)
ROMIAC	0.24	1.61[a]	1.0[a]	1.0	1.14, 1.17[b]		1.7–3	13.3–34.3	4.4–20	0.4–1.4[c]	1.16–20[a]	Mui et al. (2013) This study

[a]Nominal value.
[b]$f_{Z,E}$ values for ROMIAC1 and ROMIAC2, respectively.
[c]$\mathcal{R}/\mathcal{R}_{nd,eff}$ values range from 0.35 to 1.07.

to model the *intrinsic* classification region transmission of particles. However, the resulting L_{eff} value cannot be compared directly to those calculated for DMAs owing to the additional losses in the ROMIAC. In contrast to the DMA classification region, where particle trajectories at peak efficiency are far from walls, the trajectories in an OMAC are close to walls and, therefore, have non-negligible losses inside the classification region; these losses are not properly accounted for by the Stolzenburg derivation of the transfer function used for data inversion in this study. Nonetheless, the ROMIAC has demonstrated η_{trans} up to 0.49 for sub-2 nm particles.

The flow rates and resolutions used in this study fall within the range of those typically used in many other classifiers. The present ROMIAC was designed for a non-diffusive resolution comparable to that commonly used in DMAs. The ROMIAC attains apparent $\mathcal{R}/\mathcal{R}_{nd,nom}$ values well above unity, though, after correcting for β_{eff}, $\mathcal{R}/\mathcal{R}_{nd,eff}$ values range from 0.35 to 1.07. The particle diameter ranges in this study are on the lower end of those commonly probed with DMAs, as the ROMIAC was designed with the purpose of sub-20 nm classification.

6. Conclusions

This study demonstrates the ability of the ROMIAC to classify particles ranging from 1.16 to 20 nm in diameter over a wide range of classifier operating resolutions, while using cross-flow rates less than 40 lpm in a compact package. Additionally, experimental results validate empirical relationship dependencies derived from finite element simulations when geometry, flows, and electric field details are accurately captured. The relative resolution of the ROMIAC has little variation over a mobility span of three orders of magnitude, whereas that of a DMA varies by a factor of 2–3 at a flow ratio of 10, thus validating the broader dynamic range of OMAC-type instruments.

Analytical models of particle classifiers, such as those of Knutson and Whitby (1975), Stolzenburg (1988), and Flagan (2004) are applicable for instruments whose design and operation satisfy the assumptions on which those predictions are based, but geometric and experimental factors, i.e., small aspect ratios and field nonidealities, can lead to deviations in instrument behavior from such models, as seen both in this study and others (Rosell-Llompart et al. 1996; Zhang and Flagan 1996; Chen et al. 1998; Karlsson and Martinsson 2003; Brunelli et al. 2009; Jiang et al. 2011; Liu and Chen 2016). Owing to such deviations, one should be cautious about *a priori* predictions of performance, unless rigorous numerical models of the flows and fields within the instrument are available.

Finite element simulations enabled the design of an OMAC-type classifier that attains specified performance levels; similar fidelity is anticipated for other instruments, as has been previously demonstrated in the design of cylindrical and radial DMAs (Chen et al. 1998; Brunelli et al. 2009). The ROMIAC prototype described in this study attained resolutions up to ~20; the first description of the OMAC (Flagan 2004) suggested that the attainable resolution can be much greater, and the use of computational simulation tools would be the recommended approach for development of a high-resolution OMAC. These simulations can also reduce the dependence on experimental calibrations, provided sufficient computational resources are available to minimize the effects of numerical diffusion.

The ROMIAC presented here offers moderately high-resolution particle sizing through the low nanometer/gas ion regime at modest flow rates, making it a viable instrument for the study of new particle formation, atmospheric particle growth rates, and ultrafine particle inhalation exposure. To characterize the instrument over the range of particle sizes and operating conditions explored, a number of correction factors were made to the highly idealized model first proposed for the OMAC in order to account for the substantial deviations of the design from the assumptions behind the simplistic model. Nonetheless, the instrument performs as designed; empirical corrections based on calibration studies are consistent with those obtained from the results of the design simulations; DMAs that probe this same size range have required similar corrections for many low aspect ratio instruments. While the present instrument has been designed to probe particles in the low nanometer regime, the instrument can readily be adapted to probing particles throughout the range covered by the many different DMA designs to enable application to studies of particles in the cloud condensation nuclei and light scattering domains.

Nomenclature

Subscript 1 relates to the source ROMIAC while subscript 2 relates to the test ROMIAC, unless otherwise noted below.

b	electrode separation distance
b_{nom}	nominal electrode separation distance
Δb_{mesh}	additional electrode separation distance due to mesh offset from electrode plane
Δb_{shim}	additional electrode separation distance due to shim
b_{total}	total electrode separation distance
c	particle concentration
$\bar{c}$	velocity-weighted average particle concentration

c_{in}	particle concentration at aerosol inlet
$\overline{c}_{in}$	average particle concentration at aerosol inlet
c_{out}	particle concentration at aerosol outlet
$\overline{c}_{out}$	average particle concentration at aerosol outlet
$\mathcal{D}$	particle diffusivity
D_Z	particle electrical mobility diameter
e	elementary charge
E	electric field strength
$\vec{E}$	electric field vector
E_r	electric field strength along radial coordinate
E_z	electric field strength along axial coordinate
f	electric field nonuniformity correction factor (unity for flat electrode classifiers)
$f_{u,z}$	axial cross-flow velocity correction factor
f_Z	total mobility correction factor
$f_{Z,\text{bias}}$	mobility correction factor due to biases from aerosol introduction and cross-flow velocity
$f_{Z,E}$	mobility correction factor due to error in estimation of electric field strength
$f_{Z,E,\text{ROMIAC1}}$	mobility correction factor due to error in estimation of electric field strength for ROMIAC1
$f_{Z,E,\text{ROMIAC2}}$	mobility correction factor due to error in estimation of electric field strength for ROMIAC2
f_β	flow rate ratio correction factor
$f_{\tilde{\sigma}}$	dimensionless diffusion parameter correction factor
$\mathbf{F}_D$	drag force
$\mathbf{F}_E$	electric force
G	geometry factor
k	Boltzmann constant
L	axial DMA electrode length or rectilinear OMAC electrode length
L_{eff}	effective classifier length
n_{eff}	effective source distribution
n_s	source mobility distribution
Pe_{mig}	migration Péclet number
Q	volumetric flow rate
Q_a	volumetric incoming aerosol flow rate
Q_c	volumetric outgoing classified aerosol flow rate
Q_{cf}	volumetric OMAC cross-flow rate
Q_{ex}	volumetric DMA excess flow rate
Q_{sh}	volumetric DMA sheath flow rate
r	radial coordinate
$\mathcal{R}$	resolution
$\mathcal{R}_{nd}$	non-diffusive resolution
$\mathcal{R}_{nd,eff}$	effective non-diffusive resolution
$\mathcal{R}_{nd,nom}$	nominal non-diffusive resolution
R_1	central electrode radius of a cylindrical DMA
R_2	outer electrode radius of a cylindrical DMA
R_{elec}	radius of ROMIAC electrode
$R_{elec,avg}$	average of the electrode radii
$R_{elec,in}$	radius of incoming cross-flow ROMIAC electrode (lower electrode in figures)
$R_{elec,out}$	radius of outgoing cross-flow ROMIAC electrode (upper electrode in figures)
R_o	radius of aerosol outlet
T	temperature
u_a	aerosol flow fluid velocity
u_{cf}	cross-flow fluid velocity
u_r	radial fluid velocity
u_z	axial fluid velocity
$\overline{u}_z$	nominal average axial fluid velocity
$\overline{u}_{z,eff}$	azimuthally-averaged effective axial fluid velocity
$\vec{v}$	particle velocity vector
v_{mig}	particle electrical migration velocity
V	voltage applied to classifier
z	axial coordinate
Z	particle electrical mobility
$\Delta Z_{50\%}$	range of electrical mobilities transmitted with at least 50% of the efficiency of Z^*
Z^*	particle electrical mobility following characteristic trajectory
Z^*_{eff}	effective particle electrical mobility at peak efficiency
Z^*_{ideal}	particle electrical mobility suggested by idealized classifier behavior models
$\tilde{Z}$	dimensionless particle electrical mobility
$\tilde{Z}_{eff}$	effective dimensionless particle electrical mobility (incorporating f_Z)
Z_{peak}	particle electrical mobility at peak efficiency
α	aspect ratio; classification channel length to width ratio
β	aerosol flow rate to cross-flow (or sheath flow) rate ratio
β_{eff}	effective aerosol flow rate to cross-flow (or sheath flow) rate ratio
β_{nom}	nominal aerosol flow rate to cross-flow (or sheath flow) rate ratio
δ	aerosol flow rate imbalance ratio
Γ	particle stream function
$\tilde{\sigma}$	dimensionless diffusion parameter
$\tilde{\sigma}_{eff}$	effective dimensionless diffusion parameter
$\tilde{\sigma}^2_{distor}$	particle-size-independent dispersion contribution due to flow distortions

η_{charge}	charging probability
η_{det}	detector counting efficiency
η_{trans}	classifier transmission efficiency
ϕ	electric flux function
$\Delta\phi$	electric flux difference
$\Delta\phi^*$	electric flux difference for a particle of mobility Z^* traversing classifier
ψ	fluid stream function
ψ_1	fluid stream function at aerosol-inlet electrode
$\Delta\psi^*$	fluid streamline difference for a particle of mobility Z^* traversing classifier
Ω	transfer function
Ω_{eff}	effective transfer function
ξ	centered and scaled $\tilde{Z}$

Acknowledgments

The authors thank Daniel Thomas, Amanda Grantz, Ranganathan Gopalakrishnan, Paula Popescu, Johannes Leppä, and Natasha Hodas for helpful discussions. Andrew Metcalf and Xerxes López-Yglesias are acknowledged for their assistance with the particle trajectory simulations and LabView controls.

Funding

This research was supported by National Science Foundation Grant No. CBET-1236909 and a National Science Foundation Graduate Research Fellowship under Grant No. DGE-1144469 (W.M.), and the Jacobs Institute for Molecular Engineering for Medicine (R.C.F. and A.J.D.).

ORCID

Wilton Mui http://orcid.org/0000-0003-3065-1296
Richard C. Flagan http://orcid.org/0000-0001-5690-770X

References

Birmili, W., Stratmann, F., Wiedensohler, A., Covert, D., Russell, L. M., and Berg, O. (1997). Determination of Differential Mobility Analyzer Transfer Functions using Identical Instruments in Series. *Aerosol Sci. Technol.*, 27(2):215–223.

Brunelli, N. A., Flagan, R. C., and Giapis, K. P. (2009). Radial Differential Mobility Analyzer for one Nanometer Particle Classification. *Aerosol Sci. Technol.*, 43(1):53–59.

Chen, D.-R., Pui, D. Y. H., Hummes, D., Fissan, H., Quant, F. R., and Sem, G. J. (1998). Design and Evaluation of a Nanometer Aerosol Differential Mobility Analyzer (Nano-DMA). *J. Aerosol Sci.*, 29(5–6):497–509.

Cheng, Y.-S. (2001). Condensation Detection and Diffusion Size Separation Techniques, in *Aerosol Measurement: Principles, Techniques, and Applications*. 2nd ed. P. A. Baron, and K. Willeke, eds., John Wiley & Sons, Inc., New York, pp. 569–601.

Downard, A. J., Dama, J. F., and Flagan, R. C. (2011). An Asymptotic Analysis of Differential Electrical Mobility Classifiers. *Aerosol Sci. Technol.*, 45(6):717–729.

Erikson, H. A. (1921). The Change of Mobility of the Positive Ions in Air with Age. *Am. Phys. Soc.*, 18(2):100–101.

Fissan, H., Hummes, D., Stratmann, F., Büscher, P., Neumann, S., Pui, D. Y. H., and Chen, D. (1996). Experimental Comparison of Four Differential Mobility Analyzers for Nanometer Aerosol Measurements. *Aerosol Sci. Technol.*, 24 (1):1–13.

Fissan, H., Pöcher, A., Neumann, S., Boulaud, D., and Pourprix, M. (1998). Analytical and Empirical Transfer Functions of a Simplified Spectrometre de Mobilite Electrique Circulaire (SMEC) for Nano Particles. *J. Aerosol Sci.*, 29 (3):289–293.

Flagan, R. C. (1998). History of Electrical Aerosol Measurements. *Aerosol Sci. Technol.*, 28(4):301–380.

Flagan, R. C. (1999). On Differential Mobility Analyzer Resolution. *Aerosol Sci. Technol.*, 30(6):556–570.

Flagan, R. C. (2004). Opposed Migration Aerosol Classifier (OMAC). *Aerosol Sci. Technol.*, 38(9):890–899.

Franchin, A., Downard, A. J., Kangasluoma, J., Nieminen, T., Lehtipalo, K., Steiner, G., Manninen, H. E., Petäjä, T., Flagan, R. C., and Kulmala, M. (2016). A New High Transmission Inlet for the Caltech Nano-RDMA for Size Distribution Measurements of sub-3 nm Ions at Ambient Concentrations. *Atmos. Meas. Tech.*, 9(6):2709–2720.

Hagwood, C., Sivathanu, Y., and Mulholland, G. (1999). The DMA Transfer Function with Brownian motion a trajectory/Monte-Carlo Approach. *Aerosol Sci. Technol.*, 30 (1):40–61.

Hogan, C. J., and de la Mora, J. F. (2010). Ion-Pair Evaporation from Ionic Liquid Clusters. *J. Am. Soc. Mass Spectrom.*, 21:1382–1386.

Hogan, C. J., and de la Mora, J. F. (2011). Ion Mobility Measurements of Nondenatured 12-150 kDa Proteins and Protein Multimers by Tandem Differential Mobility Analysis-Mass Spectrometry (DMA-MS). *J. Am. Soc. Mass Spectrom.*, 22(1):158–172.

Jiang, J., Attoui, M., Heim, M., Brunelli, N. A., McMurry, P. H., Kasper, G., Flagan, R. C., Giapis, K., and Mouret, G. (2011). Transfer Functions and Penetrations of Five Differential Mobility Analyzers for sub-2 nm Particle Classification. *Aerosol Sci. Technol.*, 45(4):480–492.

Karlsson, M. N. A., and Martinsson, B. G. (2003). Methods to Measure and Predict the Transfer Function Size Dependence of Individual DMAs. *J. Aerosol Sci.*, 34(5):603–625.

Knutson, E. O., and Whitby, K. T. (1975). Aerosol Classification by Electrical Mobility: Apparatus, Theory, and Applications. *J. Aerosol Sci.*, 6:443–451.

Kousaka, Y., Okuyama, K., Adachi, M., and Mimura, T. (1986). Effect of Brownian Diffusion on Electrical Classification of Ultrafine Aerosol Particles in Differential Mobility Analyzer. *J. Chem. Eng. Jpn.*, 19(5):401–407.

Labowsky, M., and de la Mora, J. F. (2006). Novel Ion Mobility Analyzers and Filters. *J. Aerosol Sci.*, 37(3):340–362.

Liu, Q., and Chen, D.-R. (2016). Experimental Evaluation of Miniature Plate DMAs (mini-plate DMAs) for Future Ultrafine Particle (UFP) Sensor Network. *Aerosol Sci. Technol.*, 50(3):297–307.

Mai, H. (2016). Personal communication.

Martínez-Lozano, P., and de la Mora, J. F. (2006). Resolution Improvements of a Nano-DMA Operating Transonically. *J. Aerosol Sci.*, 37(4):500–512.

Martínez-Lozano, P., Labowsky, M., and de la Mora, J. F. (2006). Experimental Tests of a Nano-DMA with no Voltage Change between Aerosol Inlet and Outlet Slits. *J. Aerosol Sci.*, 37(11):1629–1642.

Mui, W., Thomas, D. A., Downard, A. J., Beauchamp, J. L., Seinfeld, J. H., and Flagan, R. C. (2013). Ion Mobility-Mass Spectrometry with a Radial Opposed Migration Ion and Aerosol Classifier (ROMIAC). *Anal. Chem.*, 85:6319–6326.

Oberreit, D. R., McMurry, P. H., and Hogan, C. J. (2014). Mobility Analysis of 2 nm to 11 nm Aerosol Particles with an Aspirating Drift Tube Ion Mobility Spectrometer. *Aerosol Sci. Technol.*, 48(1):108–118.

Oberreit, D. R., Rawat, V. K., Larriba-Andaluz, C., Ouyang, H., McMurry, P. H., and Hogan, C. J. (2015). Analysis of Heterogeneous Water Vapor Uptake by Metal Iodide Cluster Ions via Differential Mobility Analysis-Mass Spectrometry. *J. Chem. Phys.*, 143(104204):1–11.

Rosell-Llompart, J., Loscertales, I. G., Bingham, D., and de la Mora, J. F. (1996). Sizing Nanoparticles and Ions with a Short Differential Mobility Analyzer. *J. Aerosol Sci.*, 27 (5):695–719.

Rosser, S., and de la Mora, J. F. (2005). Vienna-Type DMA of High Resolution and High Flow Rate. *Aerosol Sci. Technol.*, 39(12):1191–1200.

Rus, J., Moro, D., Sillero, J. A., Royuela, J., Casado, A., Estevez-Molinero, F., and de la Mora, J. F. (2010). IMS-MS Studies Based on Coupling a Differential Mobility Analyzer (DMA) to Commercial API-MS Systems. *Int. J. Mass Spectrom.*, 298(1–3):30–40.

Stolzenburg, M. R. (1988). *An Ultrafine Aerosol Size Distribution Measuring System*. Ph.D. Thesis, University of Minnesota.

Tammet, H. (2003). Method of Inclined Velocities in the Air Ion Mobility Analysis, in *Proceedings of the 12th International Conference on Atmospheric Electricity*. Vol. 1, pp. 399–402.

Tammet, H. (2011). Symmetric Inclined Grid Mobility Analyzer for the Measurement of Charged Clusters and Fine Nanoparticles in Atmospheric Air. *Aerosol Sci. Technol.*, 45 (4):468–479.

Ude, S., and de la Mora, J. F. (2005). Molecular Monodisperse Mobility and Mass Standards from Electrosprays of Tetra-Alkyl Ammonium Halides. *J. Aerosol Sci.*, 36(10):1224–1237.

Winklmayr, W., Reischl, G. P., Lindner, A. O., and Berner, A. (1991). A New Electromobility Spectrometer for the Measurement of Aerosol Size Distributions in the Size Range from 1 to 1000 nm. *J. Aerosol Sci.*, 22(3):289–296.

Zhang, S.-H., Akutsu, Y., Russell, L. M., Flagan, R. C., and Seinfeld, J. H. (1995). Radial Differential Mobility Analyzer. *Aerosol Sci. Technol.*, 23(3):357–372.

Zhang, S.-H., and Flagan, R. C. (1996). Resolution of the Radial Differential Mobility Analyzer for Ultrafine Particles. *J. Aerosol Sci.*, 27(8):1179–1200.